Dirac-Hartree-Bogoliubov calculation for spherical and deformed hot nuclei: Temperature dependence of the pairing energy and gaps, nuclear deformation, nuclear radii, excitation energy, and entropy

R. Lisboa[*]

Universidade Federal do Rio Grande do Norte, Escola de Ciências e Tecnologia, 59078-970 Natal, Rio Grande do Norte, Brazil

M. Malheiro and B. V. Carlson

Departamento de Física, Instituto Tecnológico da Aeronáutica, Centro Técnico Aeroespacial,
12228-900 São José dos Campos, São Paulo, Brazil

Background: Unbound single-particle states become important in determining the properties of a hot nucleus as its temperature increases. We present relativistic mean field (RMF) for hot nuclei considering not only the self-consistent temperature and density dependence of the self-consistent relativistic mean fields but also the vapor phase that takes into account the unbound nucleon states.

Purpose: The temperature dependence of the pairing gaps, nuclear deformation, radii, binding energies, entropy, and caloric curves of spherical and deformed nuclei are obtained in self-consistent RMF calculations up to the limit of existence of the nucleus.

Method: We perform Dirac-Hartree-Bogoliubov (DHB) calculations for hot nuclei using a zero-range approximation to the relativistic pairing interaction to calculate proton-proton and neutron-neutron pairing energies and gaps. A vapor subtraction procedure is used to account for unbound states and to remove long range Coulomb repulsion between the hot nucleus and the gas as well as the contribution of the external nucleon gas.

Results: We show that p-p and n-n pairing gaps in the $^1S_0$ channel vanish for low critical temperatures in the range $T_{c^p} \approx 0.6$–1.1 MeV for spherical nuclei such as ^{90}Zr, ^{124}Sn, and ^{140}Ce and for both deformed nuclei ^{150}Sm and ^{168}Er. We found that superconducting phase transition occurs at $T_{c^p} = 1.03\Delta_{pp}(0)$ for ^{90}Zr, $T_{c^p} = 1.16\Delta_{pp}(0)$ for ^{140}Ce, $T_{c^p} = 0.92\Delta_{pp}(0)$ for ^{150}Sm, and $T_{c^p} = 0.97\Delta_{pp}(0)$ for ^{168}Er. The superfluidity phase transition occurs at $T_{c^p} = 0.72\Delta_{nn}(0)$ for ^{124}Sn, $T_{c^p} = 1.22\Delta_{nn}(0)$ for ^{150}Sm, and $T_{c^p} = 1.13\Delta_{nn}(0)$ for ^{168}Er. Thus, the nuclear superfluidity phase—at least for this channel—can only survive at very low nuclear temperatures and this phase transition (when the neutron gap vanishes) always occurs before the superconducting one, where the proton gap is zero. For deformed nuclei the nuclear deformation disappear at temperatures of about $T_{c^s} = 2.0$–4.0 MeV, well above the critical temperatures for pairing, T_{c^p}. If we associate the melting of hot nuclei into the surrounding vapor with the liquid-gas phase transition our results indicate that it occurs at temperatures around $T = 8.0$–10.0 MeV, somewhat higher than observed in many experimental results.

Conclusions: The change of the pairing fields with the temperature is important and must be taken into account in order to define the superfluidity and superconducting phase transitions. We obtain a Hamiltonian form of the pairing field calibrated by an overall constant c_{pair} to compensate for deficiencies of the interaction parameters and of the numerical calculation. When the pairing is not zero, the states close to the Fermi energy make the principal contribution to the anomalous density that appears in the pairing field. By including temperature through the use of the Matsubara formalism, the normal and anomalous densities are multiplied by a Fermi occupation factor. This leads to a reduction in the anomalous density and in the pairing as the temperature increases. When the temperature increases ($T \geqslant 4$ MeV), the effects of the vapor phase that take into account the unbound nucleon states become important, allowing the study of nuclear properties of finite nuclei from zero to high temperatures.

I. INTRODUCTION

The study of nuclear properties at nonzero temperatures has been investigated since the pioneering works [1–4] describing the formation and decay of a compound nucleus induced by light projectiles in nuclear reactions. In the last years nuclear reactions involving high-energy projectiles and heavy ions producing a variety of excited nuclei have been investigated [1,5–8]. Construction of the caloric curve furnishes one

possible way of comparing nuclear temperatures and excitation energies [7]. Furthermore, a possible correlation between nuclear instabilities and the liquid-gas phase transition in nuclear matter has also been suggested [1]. These studies of hot nuclei predict the existence of a liquid-gas phase transition with the signature of a large increase of the entropy and a peak in the specific heat at some critical temperature [1]. The ALADIN Collaboration presented a weak isotopic dependence of the nuclear caloric curve and a critical temperature $T \approx 5.6$ MeV of excited nuclear systems in the $A \approx 90$ region well below $T^{nm} \approx 14$ MeV calculated for nuclear matter [8]. The stability of a hot nuclear system formed in a heavy ion collision

_____
[*]ronai@ect.ufrn.br

depends on the continuum states, since the nucleus can be considered to be in thermal equilibrium with evaporated nucleons forming a surrounding gas. It was found that at temperatures above 3–4 MeV, unbound states make important contributions to the nuclear density and should be considered in the calculations [9,10]. Using the Hartree-Fock theory at finite temperature (FTHF) Bonche, Levit, and Vautherin proposed a method to consider these unbound states. Instabilities of hot nuclei due to the Coulomb interaction were also analyzed by comparison of the FTHF results of Refs. [9,10] with a semiclassical Thomas-Fermi approximation. They conclude that at low temperatures ($T \ll 2$ MeV) the subtraction procedure is also indispensable in this approximation [11–13]. They applied a gas subtraction procedure to account for the unbound states, which includes the long-range Coulomb repulsion between the hot nucleus and the gas but not that between the particles of the gas. Then, using the FTHF approach with different Skyrme interactions, they found $T = 8 \sim 10$ MeV for ^{208}Pb, depending on the interaction used [9]. These calculations allowed them to analyze binding energies, nuclear radii, densities, single-particle spectra, entropy, and level densities beyond $T = 4$ MeV, the limiting temperature used in previous works without the subtraction procedure. The first calculation based on Hartree-Bogoliubov approximation to consistently describe pairing correlations (superfluidity) in nonrelativistic nuclear matter was developed by Gogny [14,15]. This approximation was extended to a relativistic calculation by Carlson and Frederico [16] and, later, Kucharek and Ring [17], where a Dirac-Hartree-Fock-Bogoliubov equation was obtained using the Gorkov formalism [18]. These calculations furnished pairing gaps that are too large compared to later calculations, where a full Dirac structure of the self-energy and pairing fields was used in DHFB approximation [19,20]. An adequate description of the pairing interaction in nuclear matter was obtained by requiring the relativistic mean field (RMF) meson-exchange interaction to describe the low-energy two-nucleon scattering in the $^1S_0$ channel [21]. One manner of doing this is to supplement each parameter set with a high-momentum cutoff, so that it describes the two-nucleon $^1S_0$ virtual state correctly and, as a consequence, provides consistent values for the pairing gap in nuclear matter [21]. The same authors extended their calculations to finite nuclei where the pairing correlations, the nucleon, and mesons mean fields were calculated self-consistently neglecting the Fock terms, a formalism called the Dirac-Hartree-Bogoliubov (DHB) approximation [22]. The Dirac-Hartree-Bogoliubov equations in the continuum can be used to study exotic nuclei with large rms matter radius, as was first observed 15 years ago [23,24]. In the work [25] the pairing correlations and the scattering of Cooper pairs was introduced using a continuum Hartree-Bogoliubov (RCHB) in the framework of relativistic mean field theory with a density dependent force of zero range in the pairing channel adjusted to obtain the proper size of the halo ^{11}Li. This neutron halo phenomena was described in the mean field approximation, in which the last nucleons of the ^{11}Li nucleus are weakly bounded with filled orbital close to the continuum limit. The RCHB theory and associated detailed numerical techniques were developed in Refs. [26–28] to study not only stable nuclei but also the nuclei near the drip line.

In this work we extend the self-consistent DHB calculation of Ref. [22] to include finite temperature effects, considering explicitly the temperature dependence of the pairing energy and gaps [29]. Results of the temperature dependence for the pairing gap and pairing energy have been shown in our brief work [30], which neglected the vapor subtraction procedure. Later, [31] we explicitly included the contributions of the external gas in order to subtract them when calculating binding energy, nuclear radii of spherical, and deformed nuclei. We found in this later work that calculated values of the pairing gaps of ^{168}Er are $\Delta_{nn} = 0.62$ MeV and $\Delta_{pp} = 1.03$ MeV that reproduce the experimental data at $T = 0$. For this nucleus the pairing energy is $E_{\text{pair}} = -17.84$ MeV at $T = 0$ and decreases to zero at a temperature of about $T_{c^p} \approx 1.0$ MeV. Similar calculations were performed in Ref. [32], where pairing correlations were included in the constant gap approximation only for the $T = 0$ case and were ignored for $T > 0$ for open-shell nuclei, since the nuclear pairing energy vanishes at low temperatures [33–35]. These calculations furnished gap parameters for neutrons and protons of $\Delta_{nn} = 1.034$ MeV and $\Delta_{pp} = 1.176$ MeV for ^{168}Er. The authors in Ref. [32] did not show the effects of the temperature on the nuclear spectra and the shell structure of a hot nucleus. Nor did they include the effects of the pairing energy that could affect their results, since pairing is important for higher energy levels that are more sensitive to the temperature increase. They showed the finite temperature dependence of the meson mean field potentials and calculated thermodynamic effects for finite nuclei, such as deformation, excitation energy, entropy, and level density parameters at high nuclear excitations. Using a mean field approach, they found that nuclear deformation and shell effects disappear at excitations around $T_{c^s} \sim 3$ MeV for the deformed nuclei ^{168}Er and ^{168}Yb, and around $T_{c^s} \sim 2$ MeV for the nucleus ^{150}Sm. As T increases, the calculated binding energy decreases and the entropy and excitation energy increase. In Ref. [36], calculations based on finite temperature Hartree-Fock-Bogoliubov (FTHFB) theory with a Gogny force and a large configuration space also provide a good analysis of the thermodynamic effects in finite hot nuclei. By plotting excitation energy and specific heat against temperature of superdeformed nuclei they show a normal to superfluidity phase transition at a critical temperature of $T_{c^p} \approx 0.7$ MeV. In the same plots, the shape transition disappearance of the nuclear deformation occurs at $T_{c^s} \approx 2.7$ MeV.

Recently, the pairing interaction and temperature dependence of the isotopic chain for spherical nuclei was investigated in finite-temperature (FTRHB) [37] where the dependence of the pairing on temperature was calculated for several spherical nuclei based on a Gogny [38] or a separable pairing force [39] using the point-coupling interaction PC-PK1 [40]. A simple rule for evaluating the critical temperature from the adjusted neutron pairing gap to the experimental one at zero temperature was found, as $T_{c^p} = 0.6\Delta_{nn}(0)$. In particular for the nucleus ^{124}Sn, a critical temperature $T_{c^p} = 0.8$ MeV was found with a neutron pairing gap at zero temperature of $\Delta_{nn}(0) = 1.33$ MeV. This rule was also obtained in Ref. [41] where pairing field and pairing tensor were obtained from the solution of FTHFBCS model. In their calculations using Skyrme interactions, the pairing gap vanish

between 0.5 and 0.9 MeV for all Sn isotopes and the relation $T_{c^p} = 0.57\Delta_{nn}(0)$ was also found. More recently a study of pairing transition has been done in FTRHFB formalism [42] and a systematic calculation of the pairing was performed for several semimagic isotopic/isotonic chains. They found that the critical temperature for pairing transition generally follows the rule $T_c = 0.60\Delta_{nn}(0)$ with a finite-range pairing force and $T_c = 0.57\Delta_{nn}(0)$ with a constant pairing force.

It is important to stress that until now no relativistic calculations for finite nuclei exist that consider the temperature and density dependence of relativistic pairing fields obtained self-consistently have included the vapor phase to take into account the unbound nucleon states. This is done here, in a finite temperature Dirac-Hartree-Bogoliubov formalism, or FTDHB, in which we investigate the temperature dependence of pairing gaps, nuclear deformations, radii, binding energies, entropy, and the caloric curve of spherical and deformed nuclei. The RMF model used in our formalism is the nonlinear Walecka model NL3 [43], since this parameter set provides a very good description of several experimental properties of many stable nuclei. The NL3 parametrization was also used in Ref. [32], and we will compare our results with the ones obtained in this work. An overall constant c_{pair} is introduced in the expression for the pairing interaction to better reproduce the pairing gap and energies at zero temperature for finite nuclei. Furthermore, as already mentioned, the vapor subtraction procedure was used to take in account the effects of unbound states and to remove the long-range Coulomb repulsion between a hot nucleus and its gas [9,10]. In this manner, the temperature dependence of nuclear properties of finite nuclei can be studied from zero temperature to high temperatures in comparison with the studies done in Ref. [32]. We will show that p-p and n-n pairing gaps in the ${}^1S_0$ channel vanish for low temperatures in the range $T_{c^p} = 0.6$–1.1 MeV for open-shell spherical nuclei, such as ^{90}Zr, ^{124}Sn, and ^{140}Ce, and for deformed nuclei, such as ^{150}Sm and ^{168}Er. The nuclear superconducting phase transition occurs at $T_{c^p} = 0.7$ MeV for the ^{90}Zr, $T_{c^p} = 1.1$ MeV for the ^{140}Ce, $T_{c^p} = 0.9$ MeV for the ^{150}Sm, and $T_{c^p} = 1.00$ MeV for the ^{168}Er. The superfluidity phase transition occurs $T_{c^p} = 1.0$ MeV for the ^{124}Sn, $T_{c^p} = 0.6$ MeV for the ^{150}Sm, and $T_{c^p} = 0.7$ MeV for the ^{168}Er. Thus, the nuclear superfluidity phase—at least for this channel—can only survive at very low nuclear temperatures and the nuclear superconducting phase transition occurs after the superfluidity one. For these nuclei, the shell effects and nuclear deformation disappear at temperatures of $T_{c^s} = 2.0$–4.0 MeV higher than the pairing phase transition one. Our results also indicate that hot finite nuclei appear to melt into the surrounding vapor at critical temperatures in the range $T = 8.0$–12.0 MeV. It is not clear whether this merger of a hot nucleus with the surrounding vapor can be associated with a liquid-gas phase transition or not.

This paper is organized as follows: in Sec. II, we present the FTDHB formalism: in order to simplify the calculation, we exclude the Fock term and use a zero-range approximation to the relativistic pairing interaction to obtain proton-proton and neutron-neutron pairing. We introduce the temperature dependence in the Fermi occupation factor that is obtained when the integral that produces the normal and anomalous

densities in DHB theory [22] is transformed into a sum over Matsubara frequencies [44]. At end of this section we discuss the Bonche, Levit, and Vautherin gas subtraction procedure used to account for the unbound states and to remove long range Coulomb repulsion between the hot nucleus and the nucleon gas [9]. In Sec. III, we present some details about our numerical calculations following the formalism of Ref. [22] at temperature zero as well as the application of the method of Bonche, Levit, and Vautherin to solve the FTDHB formalism. In Sec. IV, we present our results concerning the ground state properties of hot nuclei. In Sec. IV A we discuss spherical and deformed nuclei. We analyzed the temperature dependence of the binding energy, the neutron and charge radii, the nuclear deformation, density, and mean field mesons and Coulomb potentials. We dedicate particular attention to the temperature dependence of the pairing gaps and pairing interaction. Finally, in Sec. IV B thermodynamical properties, such as entropy, excitation energy, and caloric curves as a function of the temperature, are also discussed for several nuclei.

II. FORMALISM

The Dirac-Hartree-Bogoliubov (DHB) formalism at zero temperature was developed in the work of Carlson and Hirata [22]. We will use the same formalism and the same structure in this work. The free Lagrangian density for the nucleon-meson many-body system is taken as

$$\mathcal{L}_0(x) = \overline{\psi}(x)[i\partial\!\!\!/ - M]\psi(x) + \tfrac{1}{2}\partial_\mu \sigma(x)\partial^\mu \sigma(x) - U[\sigma(x)]$$
$$+ \tfrac{1}{2}m_\omega^2 \omega_\mu(x)\omega^\mu(x) + \tfrac{1}{2}m_\rho^2 \vec{\rho}_\mu(x)\cdot\vec{\rho}^{\,\mu}(x)$$
$$- \tfrac{1}{4}F_{\mu\nu}F^{\mu\nu} - \tfrac{1}{4}\Omega_{\mu\nu}\Omega^{\mu\nu} - \tfrac{1}{4}\vec{G}_{\mu\nu}\cdot\vec{G}^{\mu\nu}. \quad (1)$$

The meson fields included are the isoscalar-scalar σ meson, the isoscalar-vector ω meson, the isovector-vector ρ meson, and the photon. The Lagrangian also contains a nonlinear scalar self-interaction term $U(\sigma)$ of the σ meson including cubic and quartic terms,

$$U[\sigma(x)] = \tfrac{1}{2}m_\sigma^2 \sigma(x)^2 + \tfrac{1}{3}g_3 \sigma(x)^3 + \tfrac{1}{4}g_4 \sigma(x)^4, \quad (2)$$

important for a good description of the nuclear surface. We take the interaction terms in the Lagrangian density to have the simplest possible form consistent with their Lorentz and isospin structure,

$$\mathcal{L}_{\text{int}}(x) = g_\sigma \overline{\psi}(x)\sigma(x)\psi(x) - g_\omega \overline{\psi}(x)\gamma_\mu \omega^\mu(x)\psi(x)$$
$$- \frac{1}{2}g_\rho \overline{\psi}(x)\gamma_\mu \vec{\tau}\cdot\vec{\rho}^{\,\mu}(x)\psi(x)$$
$$- e\,\overline{\psi}(x)\frac{(1+\tau_3)}{2}\gamma_\mu A^\mu(x)\psi(x). \quad (3)$$

The quantities M, m_σ, m_ω, and m_ρ are the nucleon and σ-, ω-, ρ-meson masses, respectively, while g_σ, g_ω, g_ρ, and e are the corresponding coupling constants for the mesons and the photon. The vector field tensors are defined as

$$F_{\mu\nu} = \partial_\mu A_\nu - \partial_\nu A_\mu,$$
$$\Omega_{\mu\nu} = \partial_\mu \omega_\nu - \partial_\nu \omega_\mu, \quad (4)$$
$$\vec{G}_{\mu\nu} = \partial_\mu \vec{\rho}_\nu - \partial_\nu \vec{\rho}_\mu.$$

In particular, we will not consider tensor couplings of the vector mesons nor the pseudoscalar π and η mesons. The

baryon spinor $\psi(x)$ has four Dirac components for each of the two isospin projections—$m_t = 1/2$ for protons and $m_t = -1/2$ for neutrons—for a total of eight components. To obtain a complete one-body description, we must take into account the propagation of particles and holes as well as the conversion of one to the other. A HFB formalism that succeeds in unifying these ingredients simply and clearly is the Gorkov one [18]. This is constructed in terms of the self-energy Σ, which describes the average interaction of a nucleon with the surrounding matter, and the pairing field Δ and its conjugate $\bar{\Delta}$, which describe respectively the formation and destruction of pairs during the propagation. In particular, the definitions of Δ and $\bar{\Delta}$ make use of correlated pairs of time-reversed single-particle states, in agreement with the original idea of Cooper [45]. In the Gorkov formalism, we introduce such pairs by using an extended form of the time-reversed states, which we designate by Ψ_T, where we now have as an ansatz for the effective single-particle Lagrangian

$$
\begin{aligned}
\int dt\, L_{\text{eff}} = \int d^4x\, d^4y \Big\{ &\overline{\psi}(x)[i\slashed{\partial} - M + \gamma_0\mu] \\
&\times \delta(x-y)\psi(y)\overline{\psi}(x)\Sigma(x,y)\psi(y) \\
&+ \tfrac{1}{2}\overline{\psi}(x)\Delta(x,y)\psi_T(y) + \tfrac{1}{2}\overline{\psi}_T(x)\overline{\Delta}(x,y)\psi(y) \Big\},
\end{aligned}
$$
(5)

where μ represents the chemical potential to be used as Lagrange multipliers to fix the average number of protons and neutrons.

The hole wave function Ψ_T is defined as

$$
\Psi_T = A\overline{\Psi}^{\text{T}}, \quad \overline{\Psi}_T = \Psi^{\text{T}}A^\dagger,
$$
(6)

where Ψ^{T} denotes the transpose of the wave function Ψ, and $A = \tau_2 \otimes \gamma_5 C$, in which the Pauli matrix τ_2 acts in the isospin space and C is the charge conjugation matrix. The symmetries of the effective mean-field Lagrangian under transposition, Hermitian conjugation, and the exchange of dummy variables x and y, yield the following properties of the mean fields:

$$
\begin{aligned}
\Delta(x,y) &= -A\, \Delta^{\text{T}}(x,y)\, A^\dagger = -A\, [\Delta(y,x)]^{\text{T}}\, A^\dagger, \\
\overline{\Delta}(x,y) &= -A\, \overline{\Delta}^{\text{T}}(x,y)\, A^\dagger,
\end{aligned}
$$
(7)

and

$$
\begin{aligned}
\Sigma(x,y) &= \gamma_0 \Sigma^\dagger(x,y)\gamma_0, \\
\Delta(x,y) &= \gamma_0 \overline{\Delta}^\dagger(x,y)\gamma_0.
\end{aligned}
$$
(8)

These constraints are important in limiting the possible structure of the self-energy and pairing fields.

The coupled equations of motion for the fields ψ and ψ_T that result are known as the (Dirac-)Hartree-Fock-Bogoliubov (DHFB) equations,

$$
\int d^4y \begin{pmatrix} (i\slashed{\partial} - M + \gamma_0\mu)\delta(x-y) - \Sigma(x,y) & \Delta(x,y) \\ \bar{\Delta}(x,y) & (i\slashed{\partial} + M - \gamma_0\mu)\delta(x-y) + \Sigma_{\text{T}}(x,y) \end{pmatrix} \begin{pmatrix} \psi(y) \\ \psi_{\text{T}}(y) \end{pmatrix} = 0.
$$
(9)

Defining the generalized baryon field operator as

$$
\Psi(x) = \begin{pmatrix} \psi(x) \\ \psi_{\text{T}}(x) \end{pmatrix},
$$
(10)

one obtains for the generalized baryon (quasiparticle) propagator

$$
\begin{aligned}
S(x,y) &= \begin{pmatrix} G(x,y) & F(x,y) \\ \tilde{F}(x,y) & \tilde{G}(x,y) \end{pmatrix} \\
&= -i\left\langle \begin{pmatrix} \psi(x) \\ \psi_{\text{T}}(x) \end{pmatrix} (\overline{\psi}(y), \, \overline{\psi}_{\text{T}}(y)) \right\rangle,
\end{aligned}
$$
(11)

where, by $\langle \dots \rangle$, we mean the time-ordered expectation value in the interacting nuclear matter ground state, $\langle \tilde{0}|T(\dots)|\tilde{0}\rangle$. We assume that the state $|\tilde{0}\rangle$ contains only nucleons interacting through the exchange of virtual mesons and contains no real mesons. We also assume that $|\tilde{0}\rangle$ is symmetric under rotations and translations, so that the propagator S depends only on the difference between the end points of propagation. We observe that $G(x,y)$ is the usual baryon propagator while $\tilde{G}(x,y)$ describes the propagation of baryons in time-reversed states. The off-diagonal terms of $S(x,y)$ describe the propagation of correlated baryons and are just the relativistic generalization of the anomalous propagators defined by Gorkov [18].

The self-consistency equations for the mean fields can be written in terms of the propagators as

$$
\begin{aligned}
\Sigma(x,y) = &-i\delta(x-y)\sum_j \Gamma_{j\alpha}(x) \int d^4z\, D_j^{\alpha\beta}(x-z) \\
&\times \text{Tr}[\Gamma_{j\beta}(z)G(z,z^+)] \\
&+ i\sum_j \Gamma_{j\alpha}(x)D^{\alpha\beta}(x-y)G(x,y)\Gamma_{j\beta}(y),
\end{aligned}
$$
(12)

and

$$
\Delta(x,y) = i\sum_j \Gamma_{j\alpha}(x)D_j^{\alpha\beta}(x-y)F(x,y)A\Gamma_{j\beta}^T(y)A^\dagger.
$$
(13)

We construct a static, ground-state solution to the self-consistency equations. We write the temporal Fourier transform of the full DHFB propagator as

$$
\begin{aligned}
S(\vec{x},\vec{y};\omega) &= \begin{pmatrix} G(\vec{x},\vec{y};\omega) & F(\vec{x},\vec{y};\omega) \\ \tilde{F}(\vec{x},\vec{y};\omega) & \tilde{G}(\vec{x},\vec{y};\omega) \end{pmatrix} \\
&= \sum_\alpha \begin{pmatrix} U_\alpha(\vec{x}) \\ V_\alpha(\vec{x}) \end{pmatrix} \frac{1}{\omega - \varepsilon_\alpha + i\eta} (\overline{U}_\alpha(\vec{y}), \overline{V}_\alpha(\vec{y})) \\
&+ \sum_\beta \begin{pmatrix} U_\beta(\vec{x}) \\ V_\beta(\vec{x}) \end{pmatrix} \frac{1}{\omega + \varepsilon_\beta - i\eta} (\overline{U}_\beta(\vec{y}), \overline{V}_\beta(\vec{y})).
\end{aligned}
$$
(14)

The components $U_{\alpha,\beta}$ and $V_{\alpha,\beta}$ are Dirac spinors corresponding to the normal and time reversed components, respectively,

$$\int d^3y \begin{pmatrix} \gamma_0[(\varepsilon+\mu)\delta(\vec{x}-\vec{y})-h(\vec{x},\vec{y})] & \Delta(\vec{x},\vec{y}) \\ \bar{\Delta}(\vec{x},\vec{y}) & [(\varepsilon-\mu)\delta(\vec{x}-\vec{y})+h_{\mathrm{T}}(\vec{x},\vec{y})]\gamma_0 \end{pmatrix} \begin{pmatrix} U(\vec{y}) \\ V(\vec{y}) \end{pmatrix} = 0, \quad (15)$$

where we have introduced the single-particle Hamiltonian, $h(\vec{x},\vec{y})$, given by

$$h(\vec{x},\vec{y}) = (-i\vec{\alpha}\cdot\vec{\nabla} + \beta M)\delta(\vec{x}-\vec{y}) + \beta\Sigma(\vec{x},\vec{y}), \quad (16)$$

with

$$h_{\mathrm{T}}(\vec{x},\vec{y}) = A h^T(\vec{x},\vec{y})A^\dagger \quad \text{and} \quad h(\vec{x},\vec{y}) = h^\dagger(\vec{x},\vec{y}). \quad (17)$$

The solutions to the DHFB equation occur in pairs with real eigenvalues of opposite sign and eigenvectors of the form

$$\varepsilon = \varepsilon_\alpha : \begin{pmatrix} U(\vec{y}) \\ V(\vec{y}) \end{pmatrix}, \quad \varepsilon = -\varepsilon_\alpha : \begin{pmatrix} \gamma_0 A V^*(\vec{y}) \\ \gamma_0 A U^*(\vec{y}) \end{pmatrix}. \quad (18)$$

We can thus write either the first or the second sum of Eq. (15) in terms of the eigenvectors of the other term.

The self-consistency equations can then be written as

$$\Sigma(\vec{x},\vec{y}) = \delta(\vec{x}-\vec{y})\sum_j \Gamma_{j\alpha}(\vec{x})\int d^3z\, D_j^{\alpha\beta}(\vec{x}-\vec{z})$$

$$\times \mathrm{Tr}[\Gamma_{j\beta}(\vec{z})\rho(\vec{z},\vec{z})]$$

$$- \sum_j \Gamma_{j\alpha}(\vec{x})D^{\alpha\beta}(\vec{x}-\vec{y})\rho(\vec{x},\vec{y})\,\Gamma_{j\beta}(\vec{y}), \quad (19)$$

and

$$\Delta(\vec{x},\vec{y}) = \gamma_0 \bar{\Delta}^\dagger(\vec{x},\vec{y})\gamma_0$$

$$= -\sum_j \Gamma_{j\alpha}(\vec{x})D_j^{\alpha\beta}(\vec{x}-\vec{y})\kappa(\vec{x},\vec{y})\,A\Gamma_{j\beta}^T(\vec{y})A^\dagger \quad (20)$$

where at zero temperature we have

$$\begin{pmatrix} \rho(\vec{x},\vec{y}) & \kappa(\vec{x},\vec{y}) \\ \tilde{\kappa}(\vec{x},\vec{y}) & \tilde{\rho}(\vec{x},\vec{y}) \end{pmatrix} = \sum_{\varepsilon_\gamma<0} \begin{pmatrix} U_\gamma(\vec{x}) \\ V_\gamma(\vec{x}) \end{pmatrix} (\overline{U}_\gamma(\vec{y}), \overline{V}_\gamma(\vec{y})), \quad (21)$$

with the sum running over the negative frequency solutions, $\varepsilon_\gamma < 0$ of Eq. (15). We identify the matrix elements of Eq. (21) as the component equations of the normal and anomalous densities,

$$\rho(\vec{x},\vec{y}) = \sum_{\varepsilon_\gamma<0} U_\gamma(\vec{x})\overline{U}_\gamma(\vec{y}), \quad (22)$$

$$\kappa(\vec{x},\vec{y}) = \sum_{\varepsilon_\gamma<0} U_\gamma(\vec{x})\overline{V}_\gamma(\vec{y}). \quad (23)$$

The anomalous density, in the given form, does not necessarily satisfy the antisymmetry condition of Eq. (7). We rewrite the density in a form which explicitly satisfies this condition,

$$\kappa(\vec{x},\vec{y}) = \frac{1}{2}\sum_{\varepsilon_\gamma<0}\left(U_\gamma(\vec{x})\overline{V}_\gamma(\vec{y}) - \gamma_0 A V_\gamma^*(\vec{x})U_\gamma^T(\vec{y})A^\dagger\right). \quad (24)$$

of the positive-frequency (ε_α) and negative-frequency (ε_β) solutions to the DHFB equation, Eq. (9),

When the pairing is zero, $V_\gamma = 0$ for a state of frequency $\varepsilon_\gamma = -|e_\gamma - \mu|$ with single-particle energy e_γ below the Fermi energy μ, while $U_\gamma = 0$ for a state with single-particle energy e_γ above the Fermi energy μ. When the pairing is not zero, the transition from $V_\gamma \approx 0$ to $U_\gamma \approx 0$ occurs fairly smoothly with energy in the region of the Fermi energy. The states close to the Fermi energy thus make the principal contribution to the anomalous density.

To include temperature in the model, the sum that produces the normal and anomalous densities from Eq. (21) is transformed to a sum over Matsubara's frequencies [44],

$$\begin{pmatrix} \rho(\vec{x},\vec{y};T) & \kappa(\vec{x},\vec{y};T) \\ \tilde{\kappa}(\vec{x},\vec{y};T) & \tilde{\rho}(\vec{x},\vec{y};T) \end{pmatrix}$$

$$= -\frac{1}{2}\sum_{\varepsilon_\gamma} \begin{pmatrix} U_\gamma(\vec{x}) \\ V_\gamma(\vec{x}) \end{pmatrix} (\overline{U}_\gamma(\vec{y})\,\overline{V}_\gamma(\vec{y}))\tanh\left(\frac{\varepsilon_\gamma}{2T}\right). \quad (25)$$

This expression is subtracted so as to provide the zero temperature limit given in Eq. (21). The result is

$$\begin{pmatrix} \rho(\vec{x},\vec{y};T) & \kappa(\vec{x},\vec{y};T) \\ \tilde{\kappa}(\vec{x},\vec{y};T) & \tilde{\rho}(\vec{x},\vec{y};T) \end{pmatrix}$$

$$= \sum_{\varepsilon_\gamma} \begin{pmatrix} U_\gamma(\vec{x}) \\ V_\gamma(\vec{x}) \end{pmatrix} (\overline{U}_\gamma(\vec{y}), \overline{V}_\gamma(\vec{y}))n(\varepsilon_\gamma, T), \quad (26)$$

where $n(\varepsilon_\gamma, T)$ is the Fermi occupation factor,

$$n(\varepsilon_\gamma, T) = \frac{1}{1+\exp(\varepsilon_\gamma/T)}. \quad (27)$$

Using the relation between solutions of positive and negative frequencies, Eq. (18), we can write the densities in terms of the negative frequency solutions as

$$\begin{pmatrix} \rho(\vec{x},\vec{y};T) & \kappa(\vec{x},\vec{y};T) \\ \tilde{\kappa}(\vec{x},\vec{y};T) & \tilde{\rho}(\vec{x},\vec{y};T) \end{pmatrix}$$

$$= \sum_{\varepsilon_\gamma<0}\left[\begin{pmatrix} U_\gamma(\vec{x}) \\ V_\gamma(\vec{x}) \end{pmatrix} (\overline{U}_\gamma(\vec{y}), \overline{V}_\gamma(\vec{y}))n(\varepsilon_\gamma, T) \right.$$

$$\left. + \begin{pmatrix} \gamma_0 A V_\gamma^*(\vec{x}) \\ \gamma_0 A U_\gamma^*(\vec{x}) \end{pmatrix} (V_\gamma^T(\vec{y})A^\dagger, U_\gamma^T(\vec{y})A^\dagger)n(-\varepsilon_\gamma, T) \right]. \quad (28)$$

The normal and anomalous densities are given by

$$\rho(\vec{x},\vec{y};T) = \sum_{\varepsilon_\gamma<0}\left(U_\gamma(\vec{x})\overline{U}_\gamma(\vec{y})\,n(\varepsilon_\gamma, T)\right.$$

$$\left. + \gamma_0 A V_\gamma^*(\vec{x})V_\gamma^T(\vec{y})A^\dagger\, n(-\varepsilon_\gamma, T)\right), \quad (29)$$

and

$$\kappa(\vec{x}, \vec{y}; T) = \sum_{\varepsilon_\gamma < 0} \left(U_\gamma(\vec{x}) \overline{V}_\gamma(\vec{y}) n(\varepsilon_\gamma, T) + \gamma_0 A V_\gamma^*(\vec{x}) U_\gamma^T(\vec{y}) A^\dagger n(-\varepsilon_\gamma, T) \right). \tag{30}$$

The last equation should again be antisymmetric with respect to particle exchange. This is ensured at $T = 0$ by the form of the anomalous density given in Eq. (24). The anomalous density can be written in a similar form here as

$$\kappa(\vec{x}, \vec{y}; T) = \frac{1}{2} \sum_{\varepsilon_\gamma < 0} \left\{ \left[U_\gamma(\vec{x}) \overline{V}_\gamma(\vec{y}) - \gamma_0 A V_\gamma^*(\vec{x}) U_\gamma^T(\vec{y}) A^\dagger \right] n(\varepsilon_\gamma, T) + \left[\gamma_0 A V_\gamma^*(\vec{x}) U_\gamma^T(\vec{y}) A^\dagger - U_\gamma(\vec{x}) \overline{V}_\gamma(\vec{y}) \right] n(-\varepsilon_\gamma, T) \right\}$$

$$= \frac{1}{2} \sum_{\varepsilon_\gamma < 0} \left[U_\gamma(\vec{x}) \overline{V}_\gamma(\vec{y}) - \gamma_0 A V_\gamma^*(\vec{x}) U_\gamma^T(\vec{y}) A^\dagger \right] [n(\varepsilon_\gamma, T) - n(-\varepsilon_\gamma, T)]. \tag{31}$$

The isospin structure of the self-energy and pairing fields is determined by the assumption of pure proton-proton and neutron-neutron pairing. In this case, we can reduce the densities to two distinct matrices, one for neutrons and another for protons, distinguished by the isospin index t,

$$\begin{pmatrix} \rho_t(\vec{x}, \vec{y}; T) & \kappa_t(\vec{x}, \vec{y}; T) \\ \tilde{\kappa}_t(\vec{x}, \vec{y}; T) & \tilde{\rho}_t(\vec{x}, \vec{y}; T) \end{pmatrix} = \sum_{\varepsilon_{t\gamma} < 0} \left[\begin{pmatrix} U_{t\gamma}(\vec{x}) \\ V_{t\gamma}(\vec{x}) \end{pmatrix} (\overline{U}_{t\gamma}(\vec{y}), \ \overline{V}_{t\gamma}(\vec{y})) n(\varepsilon_{t\gamma}, T) \right.$$

$$\left. + \begin{pmatrix} \gamma_0 B V_{t\gamma}^*(\vec{x}) \\ -\gamma_0 B U_{t\gamma}^*(\vec{x}) \end{pmatrix} (V_{t\gamma}^T(\vec{y}) B^\dagger, \ -U_{t\gamma}^T(\vec{y}) B^\dagger) n(-\varepsilon_{t\gamma}, T) \right], \tag{32}$$

where $B = \gamma_5 C$.

The normal and anomalous densities for neutrons and protons at finite temperature are thus

$$\rho_t(\vec{x}, \vec{y}; T) = \sum_{\varepsilon_{t\gamma} < 0} \left[U_{t\gamma}(\vec{x}) \overline{U}_{t\gamma}(\vec{y}) n(\varepsilon_{t\gamma}, T) \right.$$

$$\left. + \gamma_0 B V_{t\gamma}^*(\vec{x}) V_{t\gamma}^T(\vec{y}) B^\dagger n(-\varepsilon_{t\gamma}, T) \right], \quad (33)$$

and

$$\kappa_t(\vec{x}, \vec{y}; T) = \frac{1}{2} \sum_{\varepsilon_{t\gamma} < 0} \left[U_{t\gamma}(\vec{x}) \overline{V}_{t\gamma}(\vec{y}) + \gamma_0 B V_{t\gamma}^*(\vec{x}) U_{t\gamma}^T(\vec{y}) B^\dagger \right]$$

$$\times [n(\varepsilon_{t\gamma}, T) - n(-\varepsilon_{t\gamma}, T)]. \tag{34}$$

It is interesting at this point to compare the densities at $T \neq 0$ with those $T = 0$, Eq. (22), in the context of pairing. The $U_{t\gamma}(\vec{x}) \overline{U}_{t\gamma}(\vec{y})$ term in the normal density, which can be loosely interpreted as the contribution of the states below the Fermi energy, is now multiplied by a Fermi occupation factor. In addition, a term which we can loosely interpret as the contribution of the states above the Fermi energy, $\gamma_0 B V_{t\gamma}^*(\vec{x}) V_{t\gamma}^T(\vec{y}) B^\dagger$, now appears multiplied by the Fermi factor of a positive-frequency state. A simple analysis of the two Fermi occupation factors reveals that, when the pairing is zero, they reduce to the expected factor of $1/\{1 + \exp[(e_\gamma - \mu)/T]\}$, where e_γ is the single-particle energy and μ is the Fermi energy. The contributions to the anomalous density are simply multiplied by the difference between the negative- and positive-energy Fermi occupations. The difference between the two factors decreases as the temperature increases, causing a reduction in the anomalous density and in the pairing.

The densities that enter the Hartree self-energy terms are traces of the normal density that can be reduced to the following expressions:

$$\rho_s(\vec{x}) = 2 \sum_{\varepsilon_{t\gamma} < 0, t} (U_{t\gamma}^\dagger \gamma_0 U_{t\gamma} n(\varepsilon_{t\gamma}, T) + V_{t\gamma}^\dagger \gamma_0 V_{t\gamma} n(-\varepsilon_{t\gamma}, T)),$$

$$\rho_B(\vec{x}) = 2 \sum_{\varepsilon_{t\gamma} < 0, t} (U_{t\gamma}^\dagger U_{t\gamma} n(\varepsilon_{t\gamma}, T) + V_{t\gamma}^\dagger V_{t\gamma} n(-\varepsilon_{t\gamma}, T)),$$

$$\rho_3(\vec{x}) = 2 \sum_{\varepsilon_{t\gamma} < 0, t} 2m_t (U_{t\gamma}^\dagger U_{t\gamma} n(\varepsilon_{t\gamma}, T) + V_{t\gamma}^\dagger V_{t\gamma} n(-\varepsilon_{t\gamma}, T)),$$

$$\rho_c(\vec{x}) = 2 \sum_{\varepsilon_{t\gamma} < 0, t} (m_t + 1/2) (U_{t\gamma}^\dagger U_{t\gamma} n(\varepsilon_{t\gamma}, T)$$

$$+ V_{t\gamma}^\dagger V_{t\gamma} n(-\varepsilon_{t\gamma}, T)). \tag{35}$$

The Hartree contribution to the self-energy can be written in terms of these densities as

$$\beta \Sigma_H(\vec{x}) = -\beta g_\sigma \, \sigma(\vec{x}) + g_\omega \, \omega^0(\vec{x}) + \frac{g_\rho}{2} \, \tau_3 \, \rho^{00}(\vec{x})$$

$$+ e \, \frac{(1 + \tau_3)}{2} \, A^0(\vec{x}), \tag{36}$$

with

$$\omega^0(\vec{x}) = g_\omega \int d^3 z \, d_\omega^0(\vec{x} - \vec{z}) \rho_B(\vec{z}),$$

$$\rho^{00}(\vec{x}) = \frac{g_\rho}{2} \int d^3 z \, d_\rho^0(\vec{x} - \vec{z}) \rho_3(\vec{z}),$$

$$A^0(\vec{x}) = e \int d^3 z \, d_\gamma^0(\vec{x} - \vec{z}) \rho_c(\vec{z}), \tag{37}$$

$$\sigma(\vec{x}) = g_\sigma \int d^3 z \, d_\sigma(\vec{x} - \vec{z}) \rho_s(\vec{z})$$

$$= \int d^3 z \, d_\sigma^0(\vec{x} - \vec{z})[g_\sigma \rho_s(\vec{z}) - g_3 \, \sigma(\vec{x})^2 - g_4 \, \sigma(\vec{x})^3],$$

where the mesonic propagators are

$$d_j^0(\vec{x} - \vec{z}) = \frac{1}{4\pi} \frac{\exp(-m_j|\vec{x} - \vec{y}|)}{|\vec{x} - \vec{y}|}. \tag{38}$$

Here, we have written the mean field σ in terms of the free propagator and have included the nonlinear terms explicitly. The meson mean fields has the same symmetry as the densities.

The pairing field has the structure of an exchange term. We neglect its Coulomb contribution and approximate the contributions of the other mesons using the zero-range limit of the meson propagators. We also neglect the contribution of the nonlinear σ-meson terms here. The zero-range approximation greatly simplifies the numerical calculations, but must be calibrated phenomenologically. The Hamiltonian form of the pairing field is, in this case,

$$\begin{aligned}
\bar{\Delta}_t^\dagger(\vec{x}, \vec{y}) &= \gamma_0 \Delta_t(\vec{x}, \vec{y}) \gamma_0 \\
&= \delta(\vec{x} - \vec{y}) c_{\text{pair}} \left[\frac{g_\sigma^2}{m_\sigma^2} \gamma_0 \, \kappa_t(\vec{x}) \, \gamma_0 \right. \\
&\quad \left. - \left(\frac{g_\omega^2}{m_\omega^2} + \frac{(g_\rho/2)^2}{m_\rho^2} \right) \gamma_0 \gamma^\mu \, \kappa_t(\vec{x}) \, \gamma_\mu \gamma_0 \right]. \tag{39}
\end{aligned}$$

An overall constant c_{pair} has been introduced in the expression for the pairing field to compensate for deficiencies of the interaction parameters and of the numerical calculation. The necessity for such a constant is apparent from studies of pairing in nuclear matter. Nonrelativistic [46–48] and relativistic [20] calculations have verified that $^1S_0$ pairing in nuclear matter is dominated by the two-nucleon $^1S_0$ virtual state. Pairing in nuclear matter is weaker the further the $^1S_0$ virtual state is from the real axis in the complex-momentum plane. The location of the virtual state depends on the strength and form of the two-nucleon interaction and on the space of states used in the calculation. In Ref. [20], various sets of interaction parameters, even zero-range ones, were shown to

furnish mutually consistent physical values for the pairing gap function, when they were supplemented with a large momentum cutoff adjusted so as to place the two-nucleon virtual state at its physical location. We expect a condition similar to that in nuclear matter to apply here. However, as it is extremely difficult to fix the position of the two-nucleon virtual state within the harmonic oscillator basis that we use, we instead multiply the pairing field by an overall constant that we expect to be able to fix independently of the charge and mass of the systems under consideration. We emphasize that this is not a weakness of our calculations alone, but of any Hartree-(Fock)-Bogoliubov calculation using a limited space of states and an effective interaction, even those using a finite-range one. The pairing field obtained in such a calculation will depend on both the interaction and the space of states used and will usually require that one or the other of these be adjusted in order to obtain reasonable results. Here, we find it more convenient to introduce an arbitrary constant in the interaction rather than arbitrarily limit the space of states we use.

With the above simplifications in the self-energy and pairing fields, the DHFB equations for neutrons and protons reduce to local differential equations. Their Hamiltonian form is

$$\begin{pmatrix} \varepsilon + \mu_t - h_t(\vec{x}) & \bar{\Delta}_t^\dagger(\vec{x}) \\ \bar{\Delta}_t(\vec{x}) & \varepsilon - \mu_t + h_t(\vec{x}) \end{pmatrix} \begin{pmatrix} U_t(\vec{x}) \\ \gamma_0 V_t(\vec{x}) \end{pmatrix} = 0, \tag{40}$$

with

$$h_t(\vec{x}) = -i\vec{\alpha} \cdot \vec{\nabla} + \beta M^*(\vec{x}) + V_t(\vec{x}); \quad t = p, n, \tag{41}$$

where

$$M^*(\vec{x}) = M - g_\sigma \, \sigma(\vec{x}), \tag{42}$$

$$V_t(\vec{x}) = g_\omega \, \omega^0(\vec{x}) + \frac{g_\rho}{2} \, 2m_t \, \rho^{00}(\vec{x}) + e \, (1/2 + m_t) \, A^0(\vec{x}), \tag{43}$$

and $\bar{\Delta}_t^\dagger(\vec{x})$ is given in Eq. (39) after some simplifications of the anomalous density. The total energy can be written in terms of the mean fields as

$$E = \int d^3x \left[\underbrace{2 \sum_{\varepsilon_\gamma < 0, t, \varepsilon_\gamma > 0} [|U_{t\gamma}(\vec{x})|^2 (\varepsilon_{t\gamma} + \mu) n(\varepsilon_{t\gamma}, T) + |V_{t\gamma}(\vec{x})|^2 (-\varepsilon_{t\gamma} + \mu) n(-\varepsilon_{t\gamma}, T)]}_{E_{\text{part}}} \right.$$

$$\underbrace{-\frac{1}{6} g_3 \, \sigma(\vec{x})^3 - \frac{1}{4} g_4 \, \sigma(\vec{x})^4}_{E_{\sigma NL}} + \underbrace{\frac{1}{2} g_\sigma \, \sigma(\vec{x}) \, \rho_s(\vec{x})}_{E_\sigma} - \underbrace{\frac{1}{2} g_\omega \, \omega^0(\vec{x}) \, \rho_B(\vec{x})}_{E_\omega}$$

$$\left. \underbrace{-\frac{1}{2} \frac{g_\rho}{2} \, \rho^{00}(\vec{x}) \, \rho_3(\vec{x})}_{E_\rho} - \underbrace{\frac{1}{2} e \, A^0(\vec{x}) \, \rho_c(\vec{x})}_{E_{\text{Coul}}} + \underbrace{\frac{1}{2} \sum_t \text{Tr}[\bar{\Delta}_t^\dagger(\vec{x}) \kappa_t(\vec{x})]}_{E_{\text{pair}}} \right] - E_{cm}. \tag{44}$$

In the expression above, we have also subtracted the harmonic oscillator estimate of the center-of-mass energy,

$$E_{cm} = \frac{3}{4}\hbar\omega_0 \coth\left(\frac{\hbar\omega_0}{2T}\right), \tag{45}$$

where we take $\hbar\omega_0 = 41A^{-1/3}$ MeV, to obtain an expression for the total internal energy of the nucleus at finite temperature.

At temperatures above about 3–4 MeV, unbound states begin to make important contributions to the density. Bonche, Levit, and Vautherin [9,10] proposed a method to take these states into account and to extend mean field calculations to even higher temperatures. They observed that the mean field equations have two solutions for a given chemical potential and temperature. One of these can be associated with a nucleus in equilibrium with the evaporated nucleons (nucleus+gas) while the other consists of a gas of nucleons alone. They determined the properties of the hot nucleus in terms of the difference between quantities associated with the the nucleus+gas and those of the gas. Formally, this is done by defining a subtracted thermodynamic potential as the difference between that of the nucleus+gas Ω_{n+g} and that of the gas Ω_g, with the exception of the Coulomb contribution to be discussed below. In particular, the baryon and proton numbers of the hot nucleus are then found to be

$$A = \int d^3r \left[\rho_{B,n+g}(\vec{r}) - \rho_{B,g}(\vec{r})\right],$$
$$Z = \int d^3r \left[\rho_{p,n+g}(\vec{r}) - \rho_{p,g}(\vec{r})\right], \tag{46}$$

where $\rho_{B,n+g}$ and $\rho_{p,n+g}$ are the baryon and proton densities of the nucleon+gas solution, respectively, while $\rho_{B,g}$ and $\rho_{p,g}$ are the corresponding quantities for the gas solution. The energy and entropy associated with the hot nucleus are also the difference between those of the two solutions, as are quantities, such as rms radii, that depend linearly on the densities.

The Coulomb contribution to the thermodynamic potential must be treated differently due to its long range, which Bonche, Levit, and Vautherin [9,10] found it to lead to strong instabilities. They thus modified the Coulomb term so that the only Coulomb interaction that contributes is that of the protons in the hot nucleus. This is done by replacing the difference between the two Coulomb contributions in the thermodynamic potential by a term taking into account only the contribution of those protons,

$$\frac{1}{2}\int d^3r[\rho_{p,n+g}(\vec{r})V_C\rho_{p,n+g}(\vec{r}\,') - \rho_{p,g}(\vec{r})V_C\rho_{p,g}(\vec{r}\,')]$$
$$\rightarrow \frac{1}{2}\int d^3r\{[\rho_{p,n+g}(\vec{r}) - \rho_{p,g}(\vec{r})]V_C$$
$$\times [\rho_{p,n+g}(\vec{r}\,') - \rho_{p,g}(\vec{r}\,')]\}. \tag{47}$$

Note that, with this substitution, the evaporated protons of the nucleon+gas and gas solutions are still subject to the Coulomb repulsion of the hot nucleus, as would be expected for protons leaving the hot system. However, they no longer suffer Coulomb repulsion due to the other evaporated/gas protons nor do they contribute to the Coulomb energy.

III. NUMERICAL SOLUTION OF THE DHB EQUATION

We solve the Dirac-Gorkov and the Klein-Gordon equations by using the same procedure that has been used by many researchers, among them, Vautherin [49] in the nonrelativistic Hartree-Fock approximation, Ghambir *et al.* [50] in the relativistic mean field + BCS approach, and Lalazissis *et al.* [51–53] in the RHB approach. To perform the calculations, the meson fields and the nucleon wave functions are expanded in deformed bases of harmonic oscillator states as done before in relativistic mean field theory for finite nuclei [50]. In actual calculations, the expansion is truncated at a finite number of major shells, with the quantum number of the last included shell denoted by N_F in the case of the fermions and by N_B for the bosons. The maximum values are selected so as to assure the physical significance of the results obtained as we discuss in Sec. IV.

The spinors of the Dirac-Gorkov equation are expanded in terms of the eigenfunctions of an axially deformed harmonic-oscillator potential,

$$V_{osc}(r_\perp, z) = \tfrac{1}{2}M\omega_z^2 z^2 + \tfrac{1}{2}M\omega_\perp^2 r_\perp^2. \tag{48}$$

The oscillator constants are taken as

$$\beta_z = \frac{1}{b_z} = \sqrt{\frac{M\omega_z}{\hbar}}, \quad \beta_\perp = \frac{1}{b_\perp} = \sqrt{\frac{M\omega_\perp}{\hbar}}, \tag{49}$$

with volume conservation relating the two constants to that of a spherically symmetric potential $b_\perp^2 b_z = b_0^3$.

The eigenfunctions of the deformed harmonic oscillator can be written explicitly as

$$\Phi_\alpha(\vec{r}) = \psi_{n_r}^{m_l}(r_\perp)\,\psi_{n_z}(z)\frac{e^{im_l\varphi}}{\sqrt{2\pi}}\chi_{m_s}\chi_{m_t}, \tag{50}$$

where α denotes the complete set of quantum numbers (n_r, m_l, n_z, m_s, and m_t) and

$$\psi_{n_r}^{m_l}(r_\perp) = \frac{N_{n_r}^{m_l}}{b_\perp}\sqrt{2}\,\eta^{m_l/2}L_{n_r}^{m_l}(\eta)e^{-\eta/2} \quad \text{with}$$
$$\eta = \left(\frac{r_\perp}{b_\perp}\right)^2, \tag{51}$$
$$\psi_{n_z}(z) = \frac{N_{n_z}}{\sqrt{b_z}}H_{n_z}(\xi)e^{-\xi^2/2} \quad \text{with} \quad \xi = \frac{z}{b_z}.$$

In Eq. (51), $L_{n_r}^{m_l}(\eta)$ and $H_{n_z}(\xi)$ are Hermite and associated Laguerre polynomials [54], with the normalization constants, $N_{n_r}^{m_l}$ and N_{n_z}, given in Ref. [50]. In these equations, n_r and n_z are the number of nodes in the r and z directions, and m_l and m_s are the projections of angular momentum and spin on the z axis. The third component of the total angular momentum Ω_γ and the parity π are then defined as

$$\Omega_\gamma = m_l + m_s, \quad \pi = (-1)^{n_z+m_l}. \tag{52}$$

We expand the Pauli components of the Dirac spinors, $uf_{t\gamma}(r_\perp, z)$, $ug_{t\gamma}(r_\perp, z)$, $vf_{t\gamma}(r_\perp, z)$, and $vg_{t\gamma}(r_\perp, z)$, in terms of the oscillator eigenfunctions. Inserting these expansions into the Dirac-Gorkov equation, Eq. (40), we can reduce the equation to the diagonalization problem of a symmetric matrix and calculate the Hartree densities and components of the anomalous density, Eq. (35). The fields of the massive

mesons are expanded in a manner similar to the fermion expansion, with the same deformation parameter β_0 but a smaller oscillator length of $b_B = b_0/\sqrt{2}$.

To apply the method of Bonche, Levit, and Vautherin [9,10], we initiate calculation of the self-consistent nucleus+gas solution with Wood-Saxon potentials of the approximate expected depths and initiate the nucleon gas solution with no potential. At each iteration, new single-particle states are calculated using the same Fermi energies for both solutions and the potentials obtained from the previous sets of single-particle states. Iteration continues until converged solutions satisfying Eq. (46) are obtained. Since we expand the single-particle wave functions in a harmonic oscillator basis, we performed calculations with up to 30 major shells to avoid spurious edge effects as much as possible. We find the resulting densities to be in good agreement with those of Bonche, Levit, and Vautherin [10] and with Skyrme Thomas-Fermi [55] ones up to temperatures near the nuclear dissolution temperature. Above this temperature, the nucleon densities of the Bonche, Levit, and Vautherin and the Skyrme Thomas-Fermi calculations, which were performed "in a box," form a bubble, with the nucleons pressed against the edges of the box. In our calculations, the densities of the nucleon gas solution increase until there are no longer enough unoccupied states for the conditions of Eq. (46) to be fulfilled.

IV. RESULTS

A. Spherical and deformed nuclei

In this subsection we investigate the effect of temperature on the closed-shell spherical nucleus ^{208}Pb [32], the open-shell spherical nuclei ^{90}Zr [50], ^{124}Sn [42], and ^{140}Ce [50], and the deformed nuclei ^{150}Sm [32,56,57] and ^{168}Er [32,35] including major oscillator shells up to $N_f = 32$ and $N_b = 64$. We use the the nonlinear Walecka model with the NL3 interaction [43]. This interaction furnishes excellent results for the binding energies and rms radii of spherical and deformed nuclei near the stability line [22]. Moreover, we can also compare our

results with other calculations of excited nuclei found in the literature also obtained using the NL3 parameter set [32]. In our calculations, the expansion is truncated at a finite number of major shells, with the quantum number of the last included shell denoted by N_F in the case of the fermions and by N_B for the bosons [50]. We choose N_F and N_B to be sufficiently large to obtain reasonable values for the nuclear observables studied. We use different bases, $N_B = 20$ and $N_F = 10$ to $N_B = 64$ and $N_F = 32$. We checked that the intermediate basis is sufficient to achieve the convergence in our numerical calculations in order to reproduce experimental and earlier theoretical results of the literature at both low and high temperatures. The larger basis with $N_B = 80$ and $N_F = 40$ increases the computational time greatly but furnishes the binding energies, rms radii, excitation energies, and entropies that are almost the same as those obtained with the smaller basis. In all cases, the oscillator frequencies $\hbar\omega_0 = \hbar\omega_z = \hbar\omega_\perp = 41A^{-1/3}$ MeV, corresponding to an undeformed basis, were used. An overall constant c_{pair} was introduced in the pairing interaction, Eq. (39), to better reproduce the experimental pairing gaps and energies. For the closed-shell case, we used a small value of $c_{\text{pair}} = 0.01$, which results in a null pairing field, as expected for closed-shell nuclei. For the case of open-shell nuclei, the value of c_{pair} is chosen for each nucleus to reproduce the gap parameters Δ_{nn} and Δ_{pp} at $T = 0$ from the experimental odd-even mass differences [58].

In order to study the effect of temperature on the binding energy (E), we use Eq. (44). The various partial energy contributions to E are the sum of the one-particle (E_{part}), nonlinear $\sigma(E_{\sigma NL})$, $\sigma(E_\sigma)$, $\omega(E_\omega)$, $\rho(E_\rho)$, Coulomb (E_{coul}), pairing (E_{pair}), and center of mass (E_{cm}) terms. We present in Figs. 1(a) and 1(b) the results for ^{208}Pb and ^{168}Er, respectively. Other spherical and deformed nuclei show very similar behavior with a different parameter c_{pair}, and basis (N_B, N_F). Inspection of Fig. 1 shows that for a given temperature the largest contribution to the binding energy comes from the sum $E_\sigma + E_\omega$ energy terms and the one-particle term E_{part} that are multiplied by factor 0.1. In general all terms decrease in
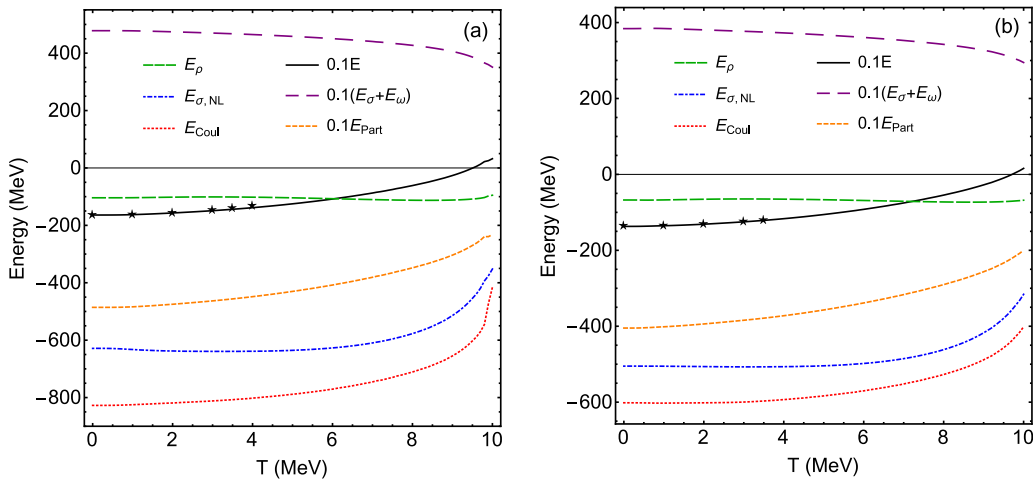

FIG. 1. Partial contributions in MeV of Eq. (44) to the binding energy E (MeV) for the nuclei (a) ^{208}Pb and (b) ^{168}Er for several values of the temperature in MeV. In plots the terms E_{part}, the sum of $(E_\sigma + E_\omega)$, and binding energy E are multiplied by factor 0.1 due to the large scale of them. The stars symbols represent the values of E that are calculated self-consistent in RMF-T for $T \leqslant 4.0$ MeV [32].

magnitude when the temperature increases, except the meson ρ (and σ_{NL}) contribution, which reach a minimum (maximum) in magnitude near $T = 3$ MeV, after which they begin to increase (decrease) for ^{208}Pb and ^{168}Er. The center of mass energy term not shown in Fig. 1, obtained from Eq. (45), is $E_{cm} = -5.19$ MeV at $T = 0$ for ^{208}Pb and is about a factor of 3 larger at $T = 10$ MeV. For ^{168}Er the center of mass contribution to the energy is $E_{cm} = -5.57$ MeV at $T = 0$ and increase by a factor of about 2.7 as the temperature increases to $T = 10$ MeV. For the two nuclei the total energy E acquires a positive value at $T = 9.5$–9.6 MeV. These results are expected because a hot nucleus becomes unstable once high temperature is reached. For ^{208}Pb the limiting temperatures obtained in Ref. [10] are $T_{lim} = 8.0$ MeV and $T_{lim} = 10.0$ MeV for effective Skyrme interactions SKM and SIII, respectively. Moreover, the Bonche procedure allows us to reach higher temperatures compared with the ones obtained not considering the vapor phase in Ref. [32] for the nuclei ^{208}Pb and ^{168}Er. For the nucleus ^{208}Pb (^{168}Er) they found at $T = 4.0$ MeV ($T = 3.5$ MeV) a binding energy of $E = -1320.4$ MeV ($E = -1208.3$ MeV), which is about 5% (0.5%) smaller than our result due to the energy of the vapor. For small temperatures $T = 0$–4 MeV the accordance of our results and the ones showed in Ref. [32] is good with a difference of less than 1% for values of E we showed by star symbols in Fig. 1. However, when the temperature increases ($T > 4$ MeV), the effects of the vapor phase becomes important.

In the case of open-shell nuclei the binding energy becomes positive for temperatures in the range $T = 10.0$–10.1 MeV for ^{90}Zr ($Z = 40$ and $N = 50$) and of $T = 9.8$–9.9 MeV for ^{140}Ce ($Z = 58$ and $N = 82$) in our calculations. A limiting temperature of $T_{lim} = 8.2$ MeV for ^{140}Ce with an excitation energy of $E^{\star} = 750.40$ MeV was reported in Ref. [11], where a Skyrme approach was used, while we obtain $E^{\star} = 739.75$ MeV at the same temperature. For the deformed nuclei ^{150}Sm we found almost the same critical temperature as the one obtained in relativistic Thomas-Fermi approximation at finite temperature using NL1

parameters [57]. The ground state experimental value of the binding energy agrees very well with our calculations [56] and the critical temperature is $T = 9$–10 MeV. This difference may be due to the parametrization we used in our calculations, which yields a slightly higher limiting temperature in our case.

The other terms that contribute to the binding energy show the same temperature behavior as those of closed-shell spherical nuclei, except for the pairing energy that, although small, is quite important. As we have already noted, the value of the pairing interaction parameter c_{pair} must be chosen to reproduce the $T = 0$ pairing gaps for neutrons Δ_{nn} and protons Δ_{pp} obtained from experimental odd-even mass tables [58] as well other observables, such as the binding energy and the charge radius. The experimental average value of the neutron gap parameter is calculated as

$$\langle \Delta_n(Z, A) \rangle = B(Z, A) - \tfrac{1}{2}[B(Z, A - 1) + B(Z, A + 1)],$$
(53)

where $B(Z, A)$ is the binding energy [58]. To reproduce the experimental results at $T = 0$ for ^{140}Ce, ^{124}Sn, and ^{90}Zr, we fix the parameter $c_{pair} = 0.60$, $c_{pair} = 0.55$, and $c_{pair} = 0.50$, respectively, with interaction NL3 [43], in Eq. (39). The bases are $(N_F, N_B) = (14, 28)$ for ^{124}Sn, $(N_F, N_B) = (32, 64)$ for ^{90}Zr and ^{140}Ce. We choose a different basis for the tin nucleus in order to be able to calculate the neutron gap parameter for all tin even isotopes as a function of the mass number (see Fig. 3). The pairing constant is taken to be $c_{pair} = 0.57$ for ^{150}Sm and $c_{pair} = 0.60$ for ^{168}Er. The bases are $(N_F, N_B) = (32, 64)$ for ^{150}Sm and ^{168}Er.

We present in Fig. 2 the variations of the (a) pairing energy and (b) gap as the temperature increases. In Fig. 2 the full lines represent Δ_{nn} and dashed lines represent Δ_{pp}. For ^{90}Zr at $T = 0$, we find $\Delta_{nn}(0) = 0$ and $\Delta_{pp}(0) = 0.681$ MeV as output of our self-consistent calculations, which provides a pairing energy of $|E_{pair}| = 4.261$ MeV. We have also studied the nucleus ^{140}Ce and obtained $\Delta_{nn}(0) = 0$ and $\Delta_{pp}(0) = 0.949$ MeV with $|E_{pair}| = 9.432$ MeV. The value $\Delta_{nn}(0) = 0$
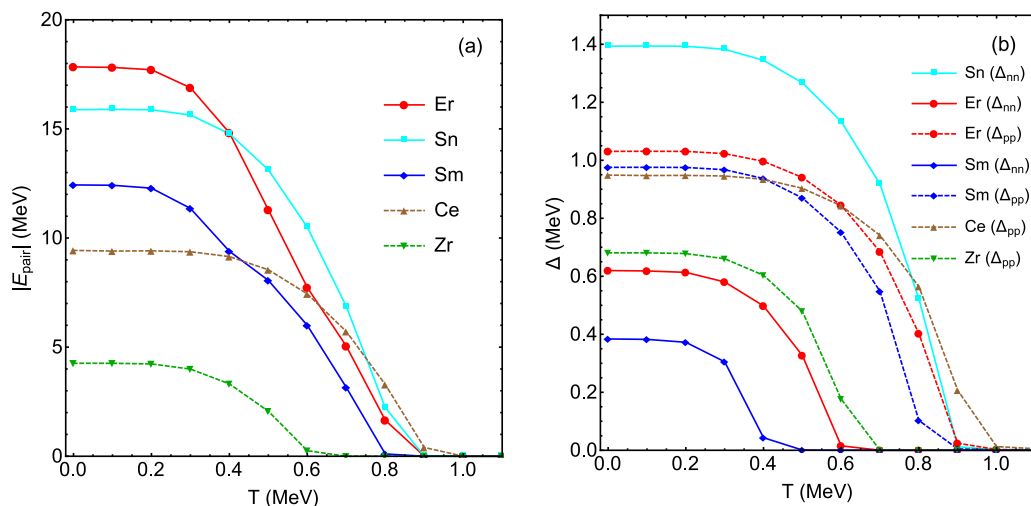

FIG. 2. Temperature dependence of the (a) pairing energy, $|E_{pair}|$ in MeV and (b) gap, Δ in MeV for the open-shell and deformed nuclei. The full lines represent Δ_{nn} and dashed lines represent Δ_{pp}.

is justified because both nuclei have a neutron close shell. The nucleus ^{124}Sn is a semimagic nucleus with a magic proton number. Thus, $\Delta_{pp} = 0$ and gap and their n-n pairing energy at zero temperature are $\Delta_{nn}(0) = 1.394$ MeV and $|E_{\text{pair}}| = 15.88$ MeV, respectively. The semimagic nuclei ^{90}Zr and ^{140}Ce with magic neutron number show a superconducting phase transition at critical temperatures $T_{c^p} \approx 0.70$ MeV and $T_{c^p} \approx 1.10$ MeV, respectively. The semimagic nucleus ^{124}Sn with magic proton number show a superfluidity phase transition at critical temperatures $T_{c^p} \approx 1.00$ MeV. It has been shown by using the BCS limit of the FTHFB equations (FTBCS) with a constant gap value that the pairing gap vanishes when the temperature increases showing a phase transition from the pair correlated phase to the normal one [33]. The author found a critical temperature of $T_{c^p} \approx 0.50$ MeV for nuclear matter. In this approximation, it is possible to show analytically that $T_{c^p} = 0.50\Delta_{nn}(0)$, where $\Delta_{nn}(0)$ is the pairing gap at $T = 0$. From Fig. 2(b) we can calculate the ratio $T_c/\Delta(0)$ for each nucleus discussed before. For ^{124}Sn we found $T_c/\Delta_{nn}(0) = 0.72$ which is different from the one obtained in the BCS approximation and reported as a phase transition from a superfluidity to normal phase obeying the rule $T_{c^p} = 0.60\Delta_{nn}(0)$ [37]. More recently a study of pairing transition has been done in FTRHFB formalism [42] and a systematic calculation of the pairing was performed for several semimagic isotopic/isotonic chains obtaining $T_{c^p} = 0.60\Delta_{nn}(0)$ for finite-range Gogny D1S interaction and $T_{c^p} = 0.57\Delta_{nn}(0)$ for zero-range density-dependent contact interaction (DDCI). They conclude the vanishing of pairing correlations at finite temperature slightly depends on the type of pairing force.

The pairing energy and gap for deformed nuclei ^{150}Sm and ^{168}Er are also shown in Fig. 2. For deformed nuclei ^{150}Sm and ^{168}Er the $\Delta_{pp}(0)$ is larger than $\Delta_{nn}(0)$ and decreases slower with temperature. For ^{150}Sm the phase transition from a superfluidity to normal phase is achieved at $T_{c^p} = 0.60$ MeV and the superconducting phase transition occurs at $T_{c^p} = 0.90$ MeV. For ^{168}Er the n-n and p-p pairing energy and gap vanish at $T_{c^p} = 0.70$ MeV and $T_{c^p} = 1.00$ MeV, respectively. Thus, in the $^1S_0$ channel the nuclear superfluidity phase can only survive at very low temperatures and the transition to normal matter occurs always in a temperature smaller than the superconducting one. Our simple rules for the critical temperature are $T_{c^p} = 1.22\Delta_{nn}(0)$ and $T_{c^p} = 0.92\Delta_{pp}(0)$ for ^{150}Sm and $T_{c^p} = 1.13\Delta_{nn}(0)$ and $T_{c^p} = 0.97\Delta_{pp}(0)$ for ^{168}Er. The different rules calculated in this work can be explained by the overall constant c_{pair} introduced in the expression for the pairing interaction, Eq. (39), to better reproduce the pairing gap and energies at zero temperature for finite nuclei. The pairing field obtained in such a calculation will depend on both the interaction and the space of states used and will usually require that one or the other of these be adjusted in order to reproduce experimental data. As we have argued in the Introduction, we find it more convenient to introduce an arbitrary constant in the interaction rather than arbitrarily limit the space of states we use. Besides, the NL3 parameter used in our relativistic calculations of the pairing field produce results that are different from the ones of [37] where the temperature dependence of the pairing was investigated by using a Gogny

or a separable pairing force based in the point-coupling interaction model PC-PK1. The authors in Ref. [42] also conclude that finite- or zero-range nature of the pairing force, while generating different density dependence pairing gaps, causes small differences in results of the ratio $T_c/\Delta(0)$.

In Fig. 3(a) the dependency the average value of the neutron gap parameter with temperature for even Sn isotopes as a function of the mass number A is presented, for the value of $c_{\text{pair}} = 0.55$ and basis with $N_F = 14$ and $N_B = 28$. The value $c_{\text{pair}} = 0.55$ was chosen to fit the ground state observables of the Sn isotopes [22]. Larger (smaller) bases than $(N_F, N_B) = (14, 28)$ raise (reduce) the pairing gaps at $T = 0$ and do not reproduce the experimental Audi-Wapstra [58] (filled circles) and the Moller-Nix [59] (open squares) values for the standard estimate of the neutron gap parameter as the difference between the binding energy of an even-even nucleus and its odd mass neighbors, Eq. (53). In Fig. 3(a) we can see for $T \leqslant 0.4$ MeV the pairing gap changes smoothly with increasing of temperature for all tin isotopes as also we can see in Fig. 2 for the nuclei ^{124}Sn, ^{168}Er, ^{150}Sm, ^{140}Ce, and ^{90}Zr. However, for $T > 0.4$ MeV the pairing gap decreases quickly when it vanishes at a critical temperature of order 0.9–1 MeV. In Fig. 3(b) we show our calculations for pairing gap energies at zero temperature (black circles) with NL3 interaction, and calculations with PKA1 (red squares), PKO1 (blue triangles), and DD-ME2 (orange diamonds) models, with the pairing channel described by Gogny pairing interaction D1S [42]. Our FTDHB results for $\Delta_{nn}(0)$ for isotopic tin are in good agreement with the results of Ref. [42]. In Fig. 3(b) we also show the critical temperature T_c (open symbols), when the pairing gap vanishes for the tin isotopic chain. These temperatures are calculated by FT-RHFB with PKA1 (open red square), PKO1 (open blue triangle), and calculated by FT-RHB with DD-ME2 (open orange diamond). For the last three models the ratio is between critical temperature and pairing gap at zero temperature $T_c/\Delta_{nn}(0) = 0.6$ for the ^{124}Sn nucleus. Our calculations produce a higher critical temperature as we see in Fig. 3(a) and as a consequence this ratio is slightly higher, $T_c/\Delta_{nn}(0) = 0.7$. In Fig. 3(a), shell closures are visible at $A = 100, 132$, and 176 and our results show that $\langle\Delta_{nn}(Z, A)\rangle$ at $T = 0$ underestimates the experimental values below the shell closure $A = 132$ and overestimates them above it. A subshell closure is also visible in the calculations, at values of the mass at which the gap parameter reaches a nonzero minimum. This is more visible when the pairing field is weaker and, thus, is more sensitive to the energy differences between the levels [22]. In our calculations this occurs at $A = 144$ ($N = 94$) and $A = 146$ ($N = 96$) just in the region where the Sn nuclei are deformed [60]. For the ^{144}Sn the deformation is $\beta = 0.0023$ at $T = 0.4$ MeV and changes to $\beta = 0.1283$ at $T = 0.5$ MeV. For the ^{146}Sn the deformation is $\beta = 0.0120$ at $T = 0.4$ MeV and changes to $\beta = 0.1224$ at $T = 0.5$ MeV. Besides for the superficial levels $2f_{5/2-}, 3p_{1/2-}$, and $3p_{3/2-}$ the single-particle energies are $\varepsilon = -1.112$ MeV, $\varepsilon = -1.215$ MeV, and $\varepsilon = -1.441$ MeV, respectively, at $T = 0.4$ MeV and change to $\varepsilon = -0.068$ MeV, $\varepsilon = -0.270$ MeV, and $\varepsilon = -0.508$ MeV at $T = 0.5$ MeV for the ^{144}Sn. A similar jump occurs for ^{146}Sn while for the nuclei ^{142}Sn and ^{148}Sn the difference between energies is almost constant.
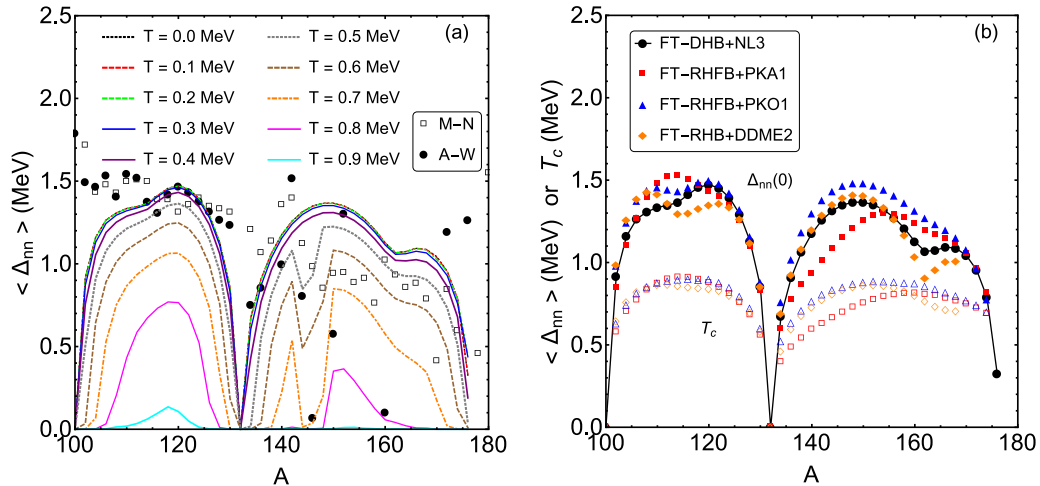
FIG. 3. (a) Evolution of neutron gap energy with temperature calculated in FT-DHB with effective interaction NL3. The experimental values are obtained from the Audi-Wapstra (filled circles) [58] and Moller-Nix [59] (open squares) mass tables at temperature zero. (b) Comparison of $\Delta_{nn}(0)$ (full symbols) and T_c (open symbols) calculated in FT-DHB with effective interaction NL3 (black circle), FT-RHFB with PKA1 and the Gogny pairing interaction D1S (red square), FT-RHFB-HFB with interaction PKO1 (blue triangle), and FT-RHB with interaction DD-ME2 (orange diamond) of Ref. [42].

We now discuss the energy spectra at several values of the temperature, for ^{40}Ca, in Fig. 4. The single-particle levels vary only slightly with temperature below $T = 1$ MeV. The lower levels acquire a minimum in the energy around $T = 2$ MeV and show a faster increase in magnitude when T increases in contrast with the levels near the chemical potential (star symbols), which show a slower variation in magnitude. These effects are similar for neutron [Fig. 4(a)] and proton [Fig. 4(b)] spectra, with the difference between them being only an

upward shift due to the Coulomb correction of about 8 MeV in the case of the protons.

The decrease of chemical potential with temperature is a manifestation of the increase of the entropy with the temperature as particles are added to the system as was found in the works [9,10]. In Fig. 5 we display the neutron spectrum of ^{208}Pb as a function of temperature into low energy [Fig. 5(a)] and high energy [Fig. 5(b)] regions due to the number of levels. We see similar behavior as in the
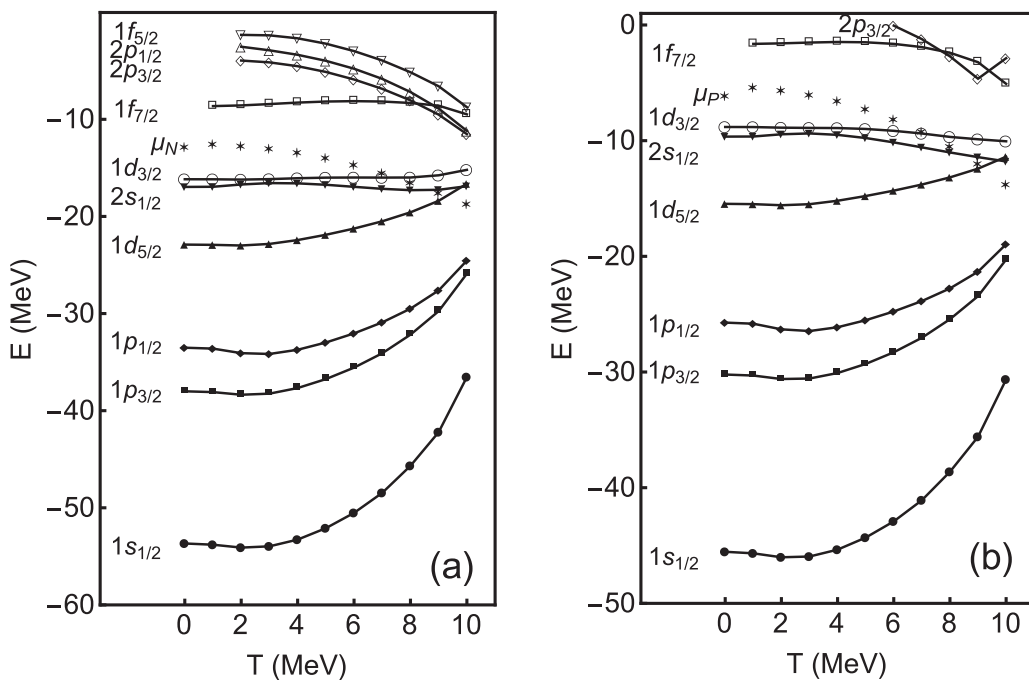

FIG. 4. (a) Neutron and (b) proton levels of ^{40}Ca as function of the temperature calculated with Bonche procedure. Levels above the chemical potential $\mu_{N,P}$ are partially occupied when $T \neq 0$.
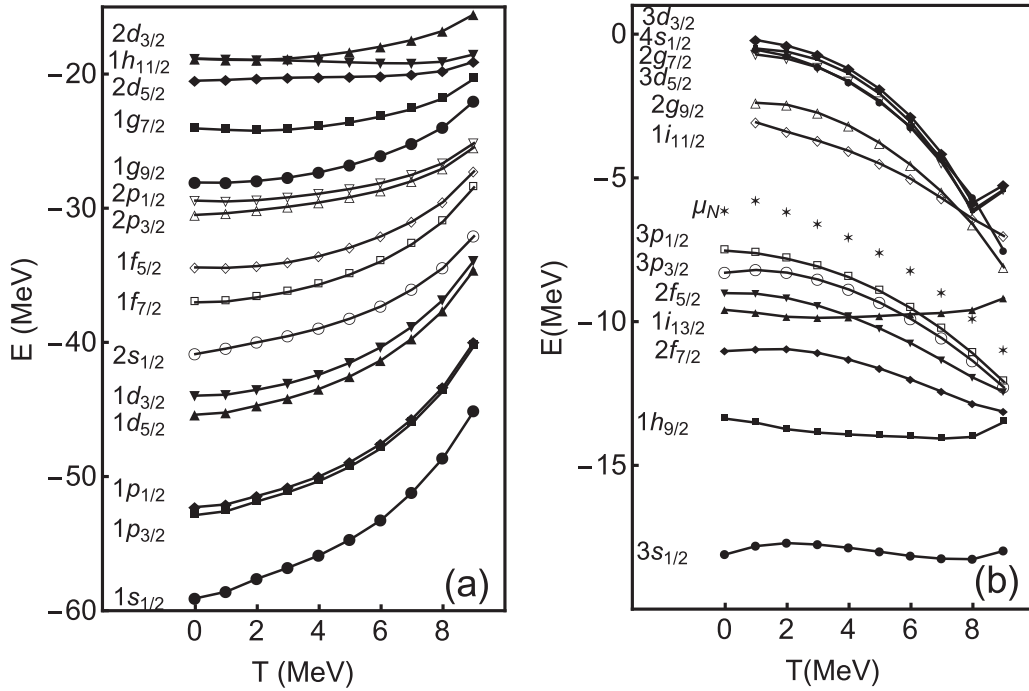
FIG. 5. The effect of the temperature in the (a) lower and (b) top levels of neutron energy spectra of ^{208}Pb. In panel (b), levels above the chemical potential (μ_N) are partially occupied when $T \neq 0$.
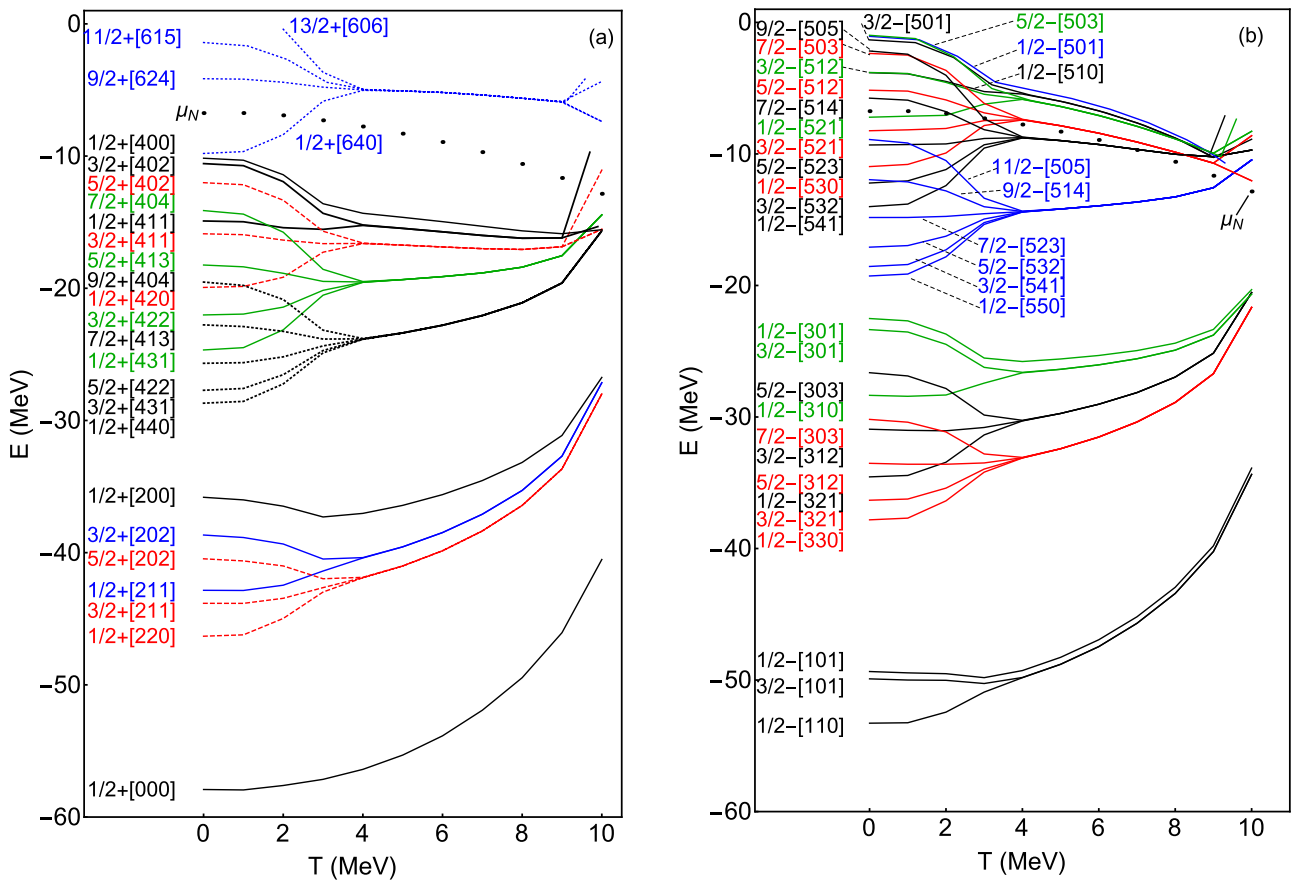

FIG. 6. The effect of temperature on the energy spectra for neutrons in (a) positive and (b) negative parity states of ^{168}Er.

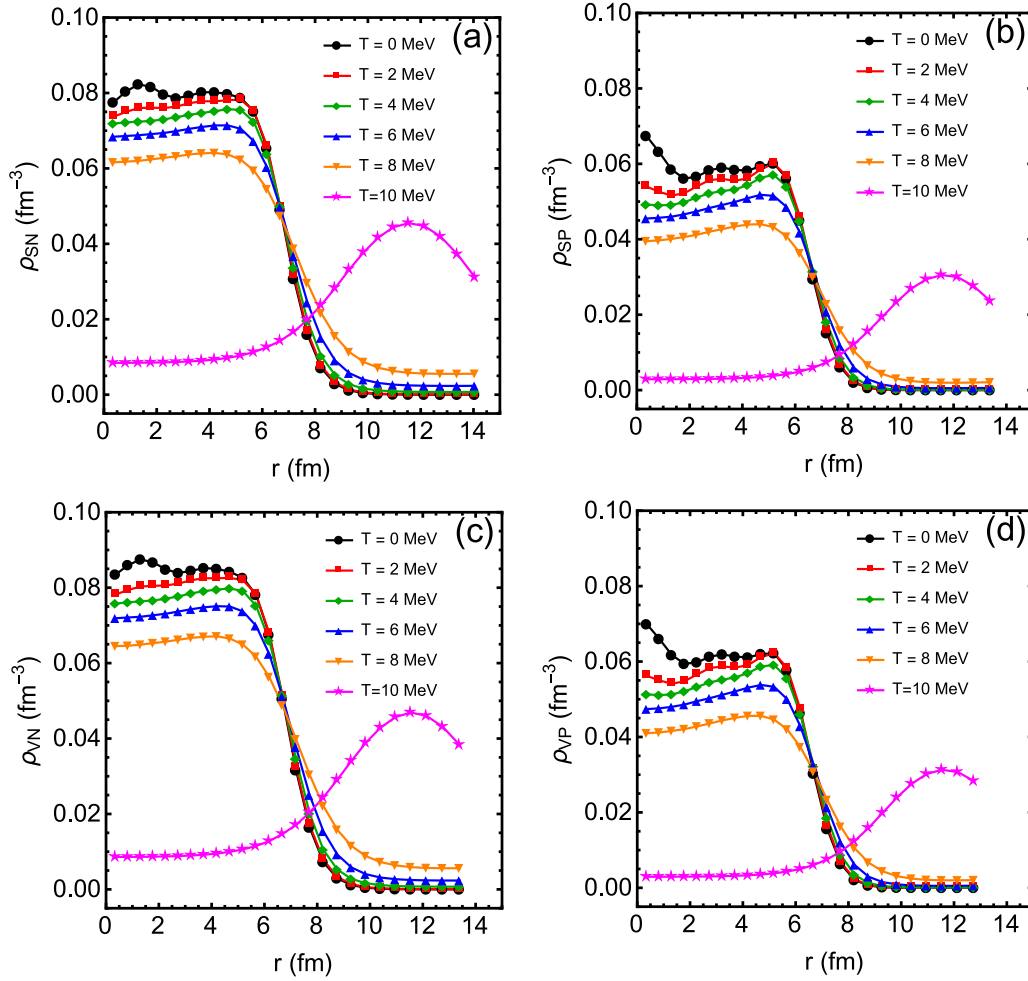FIG. 7. Nuclear densities as a function of the radius for even values of the temperature of ^{208}Pb in equilibrium with an external gas. In the top panels the scalar densities for (a) neutrons and (b) protons are displayed. In the bottom panels, the vector densities for (c) neutrons and (d) protons are shown.

case of ^{40}Ca, with the main difference being that the strong variation in the spectrum occurs only when $T > 4$ MeV. The decrease of the chemical potential with temperature seen for the nucleus ^{40}Ca and more rapidly in ^{208}Pb is a consequence of the ω potential (V_ω) that decreases with the temperature faster [see Fig. 9(b)] than increase of the single-particle energy. At zero temperature the chemical potential in RMF theories is the Fermi energy plus vector potentials $V_t(\vec{x})$ of Eq. (43). This explains why the temperature dependence of the vector potential of ω meson [dominant term of $V_t(\vec{x})$] is so important in these models to explain the chemical potential dependence with the temperature.

Furthermore, at high temperatures we see that the levels are more compressed. The temperature also affects the levels above the chemical potential, which are partially occupied when the temperature increases due to the Fermi occupation factor of nuclear densities shown in Eq. (27). The thermal energy $E \sim K_B T$ is of the order of several MeV in comparison with the difference in the energy levels of around 5 MeV at most. Thus, the nucleons in the higher levels are the most affected by the temperature and may be thermally excited to the available single-particle levels

above the chemical potential. In Fig. 6 we present the neutron energy levels of positive and negative parity for ^{168}Er as a function of the temperature. As the temperature increases, the energy levels collapse to those of a spherical nucleus near $T_{c^s} = 4$ MeV as we already related, where the shape transition takes place. The same observations can be made for ^{150}Sm, for which the pairing phase transition occurs at $T_{c^p} = 0.7$ MeV and the shape transition at $T_{c^s} = 5.1$ MeV.

We now analyze the nuclear densities of the ^{208}Pb nucleus in equilibrium with the external gas. In Fig. 7 we present (a) the scalar density for neutrons, (b) the scalar density for protons, (c) the vector density for neutrons, and (d) the vector density for protons. For each panel we plot the densities as a function of the radius for even values of the temperature in the range from $T = 0$ to $T = 10$ MeV. For all densities the magnitude of the well depth decreases and the diffusivity increases as T increases. Above $T = 2$ MeV the oscillations of the densities at the center of the nucleus due to shell effects disappear and the densities in the surface region are more sensitive to the increase of the temperature. Beyond $T \sim 9$ MeV the densities display a maximum value around $r = 12$ fm represented by stars symbols in each panel of Fig. 7.
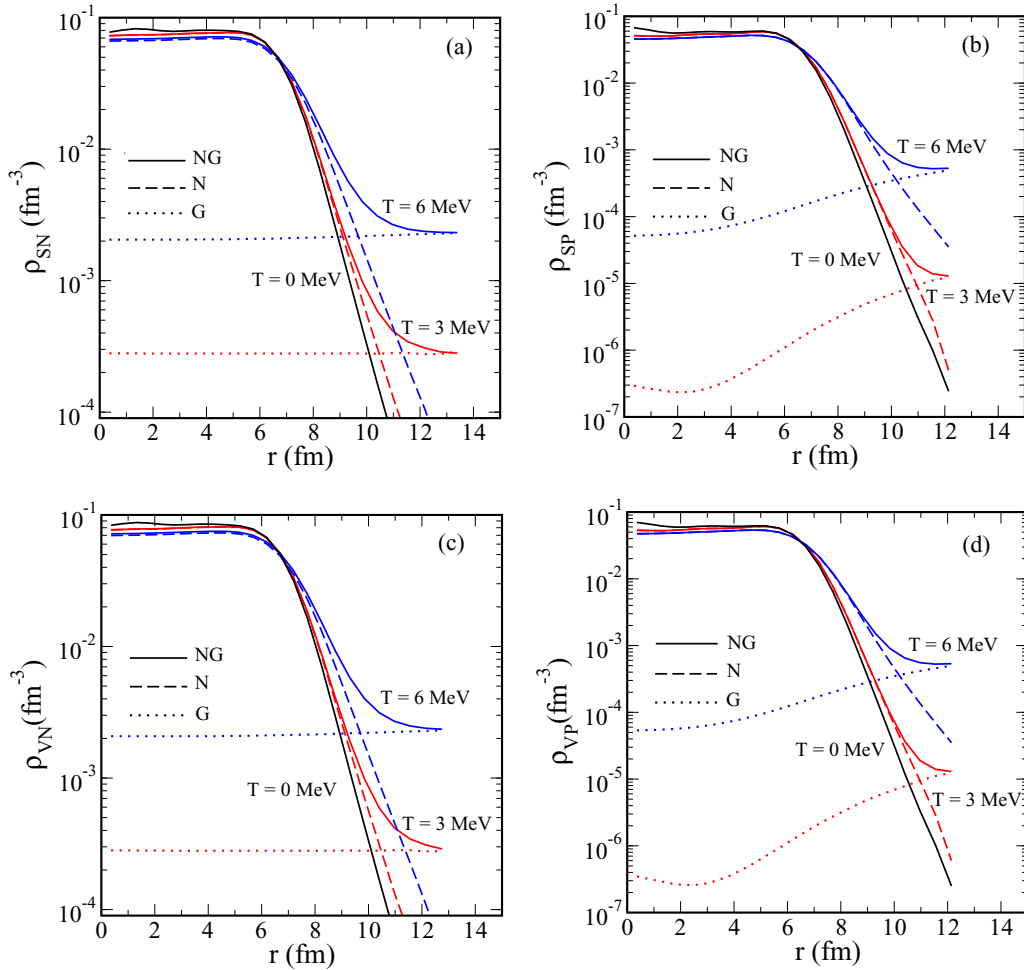
FIG. 8. Nuclear densities as a function of the radius for ^{208}Pb at three values of the temperature. In the top panels, scalar densities for (a) neutrons and (b) protons are displayed. In the bottom panels, vector densities for (c) neutrons and (d) protons are shown. The solid lines represent the nucleus+gas solution (NG), the dotted lines represent the gas alone (G), and the dashed lines represent the difference between the two—the nucleus without the gas (N).

At this high temperature, various nucleons are driven out of the nucleus and its nuclear structure is completely dissolved. These effects are most pronounced when the vapor subtraction procedure is not considered as the temperature increases. In our calculations we take this effect into account by placing the hot nucleus in equilibrium with the nucleons which are evaporated. Thus, we can remove the contribution of the gas of nucleons in the continuum in such a way that only nucleons in bound and resonant energy states are taken into account. As the temperature increases, the densities of the nucleon gas solution increase until there are no longer enough unoccupied states for the conditions of Eq. (46) to be fulfilled.

In Fig. 8 we present nuclear densities for the ^{208}Pb nucleus as a function of the radius. In each panel we present three temperatures: $T = 0, 3, 6$ MeV. The solid lines represent the nucleus in equilibrium with the external gas (nucleus+gas/NG curve) in correspondence to Figs. 7(a)–7(d). The dotted lines represent the contribution of the gas alone (gas/G curve), and the dashed lines represent the difference between the two—the nucleus without the gas (nucleus/N curve). In all panels of Fig. 8 there is only one curve for the density of the

nucleus+gas at $T = 0$ because no nucleons have evaporated this temperature. This density vanishes near $r \sim 11$ fm for neutrons and $r \sim 12$ fm for protons. The densities of the nucleus+gas (NG curves) do not go to zero at large radii when the temperature is turned on, because the gas contribution (G curves) becomes important at larger radii. When we remove the contributions of the gas, the densities of the nucleus alone (N curves) go to zero at $T \neq 0$, just like the nucleus+gas at $T = 0$. This procedure for removing the gas allows us to reach temperatures above $T = 3$ MeV up to almost $T = 10$ MeV. When the temperature increases the volume the nucleus increases and the density decreases. The nucleus disappears at temperatures above $T = 12$ MeV.

We display in Fig. 9 the radial dependence of the (a) V_σ, (b) V_ω, (c) V_ρ mean field potentials, and (d) the V_c Coulomb potential for ^{208}Pb in equilibrium with an external gas. In each panel the potential is shown at temperatures varying from $T = 0$ to $T = 10$ MeV. As was seen for the nuclear densities, the magnitudes of the well depths decrease and the diffusivity increases as T increases. Above $T = 2$ MeV the oscillations of the mean field potential well disappears and
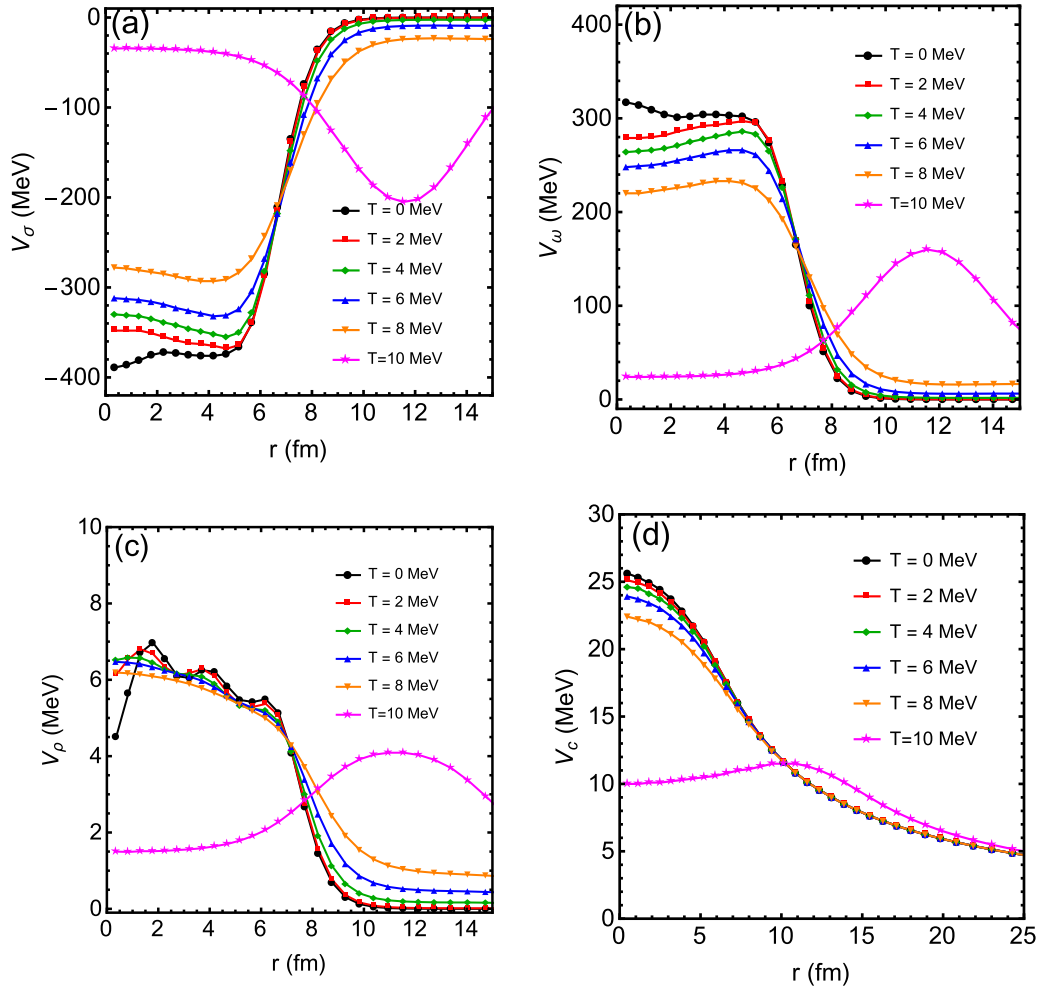
FIG. 9. Mean field potentials as a function of the radial distance for even values of the temperature of ^{208}Pb in equilibrium with an external gas. In panels (a) $V_\sigma(r)$, (b) $V_\omega(r)$, (c) $V_\rho(r)$, and (d) the Coulomb potential $V_c(r)$ are shown for ^{208}Pb.

the sensitivity to temperature of the potential in the surface region increases. At $T = 10$ MeV the potentials display a maximum in magnitude around $r = 12$ fm represented by the star symbols in all panels of Fig. 9. In Fig. 9(d) it is possible to see the long range effect of the Coulomb potential. The hot nucleus exists while the balance between surface and Coulomb contributions is maintained, as was explained in Ref. [10]. Our results extend those presented in Ref. [32], where the contribution due to evaporation of nucleons was ignored and, as a consequence, results were shown only up to $T \leqslant 4$ MeV and pairing correlations were ignored for $T \neq 0$. However, we agree with their main conclusions concerning the behavior of the nucleus as the temperature increases.

In Fig. 10(a) we show the calculated radii for deformed nucleus ^{168}Er. All radii decrease as the temperature increases and reach minimum values at $T \sim 3$ MeV before increasing at higher temperatures up to values 15%. In Fig. 10(b) the deformation β decreases more slowly with the increase in temperature. At $T \sim 3$ MeV ($T \sim 4$ MeV) the deformation vanishes for ^{150}Sm (^{168}Er) and the nucleus becomes spherical. The circle and square symbols represents the results of ^{168}Er and ^{150}Sm, respectively, from [32]. It is important to note

that the nuclear deformation is constant until the pairing energy vanishes ($T_{c^p} \sim 1$ MeV). After that, it decreases and vanishes turning the nuclei spherical. Thus, the superfluidity and the superconducting phase transition happen before the shape transition. The pairing field goes to zero at a smaller temperature than the nuclear deformation.

B. Excitation energy and entropy as function of the temperature

We will now discuss the effect of temperature on excitation energy and entropy and look for signatures of the pairing and deformation phase transitions and of nuclear dissolution in these quantities. The entropy for hot nuclei increases as the temperature increases. On the scale of Fig. 11(a), the entropy increase is almost linear with temperature for ^{40}Ca, ^{90}Zr, ^{124}Ce, ^{140}Ce, ^{168}Er, and ^{208}Pb. It is possible to identify a weak change in the slope of the entropy curve at $T \sim 2$–4 MeV for the deformed nuclei, which corresponds to the shape phase transition, and another change in slope at $T \sim 8$–10 MeV where the nuclei dissolve into the gas. To study the pairing phase transition, the plot of entropy against temperature is shown on a magnified temperature scale in Fig. 11(b). In this
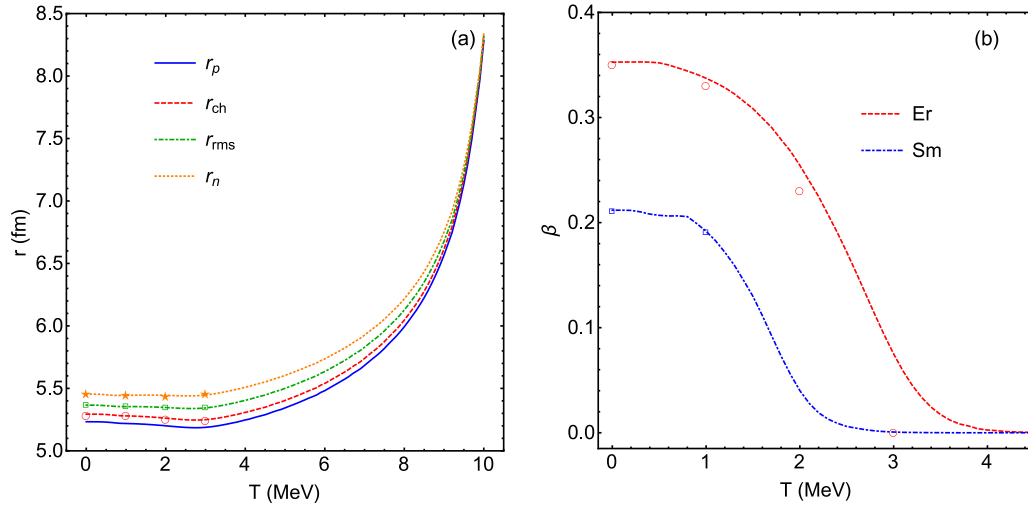
FIG. 10. (a) The charge r_{ch}, neutron r_n, proton r_p, and r_{rms} radii (fm) for ^{168}Er and (b) deformation, β for the nuclei ^{150}Sm and ^{168}Er as a function of temperature in MeV. The square and circle symbols represent calculated self-consistent RMF-T from [32].

zoom, for $0 \leqslant T \leqslant 1.5$ MeV, the curves for the deformed and open-shell spherical nuclei are no longer linear below the critical temperature T_{cp}. Thus, it is possible to clearly identify the critical temperatures of the superfluidity phase from the entropy change in agreement with those given in Fig. 2. Several recent experimental studies of the thermodynamics of finite hot nuclei have been performed by the Oslo cyclotron group [6,61–64]. They develop a thermodynamical model to investigate and classify the pairing phase transition at low temperature, $T \approx 0.5$ MeV, where the pairing interaction vanishes. Their model calculations of the heat capacity and entropy of $^{93-98}$Mo isotopes as a function of the temperature show a peak in the heat capacity and a smooth bump on the entropy curves where Cooper pairs are broken. They obtained critical temperatures in the range $T_{cp} \sim 0.7$–1.0 MeV for the $^{93-98}$Mo isotopes [63], in general agreement with our results.

In Ref. [42] similar results to the entropy as a function of the temperature were found for the nucleus ^{120}Sn. They show that the pairing correlations is clearly visible below the critical temperature, inducing a strong reduction of the entropy.

Finally, we show the caloric curve per nucleon $E^\star/A$ for spherical nuclei in Fig. 12(a) and for the deformed nuclei in Fig. 12(b). We can see that the excitation energy increases approximately quadratically with the temperature. As the curves lie close to one another, we can claim that the excitation energy per nucleon $E^\star/A$ is roughly independent of the mass number A and is a function of the temperature T alone. This is what one would expect if the nuclear equation of state were determined by the volume energy term alone. Corrections to the volume energy (surface, symmetry, Coulomb, etc.) furnish the small differences seen in the figure on the right, where the differences in mass number and charge to mass
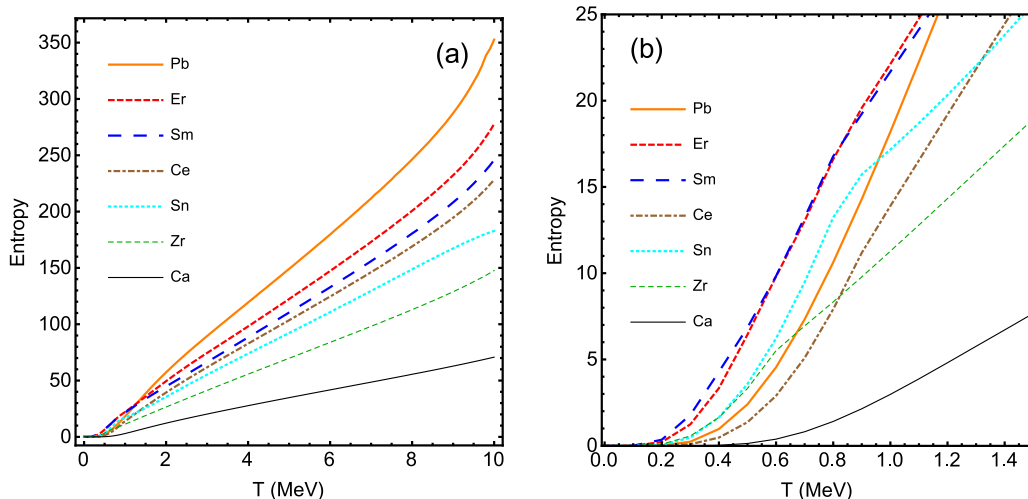

FIG. 11. The entropy as a function of the temperature for spherical and deformed nuclei. (a) Shape transitions and dissolution of the nuclei are revealed by negative and positive curvature, respectively. (b) In the zoom of temperature scale in the figure on the left, the critical temperature for the pairing transition in deformed nuclei appears as a change in slope of the curve.
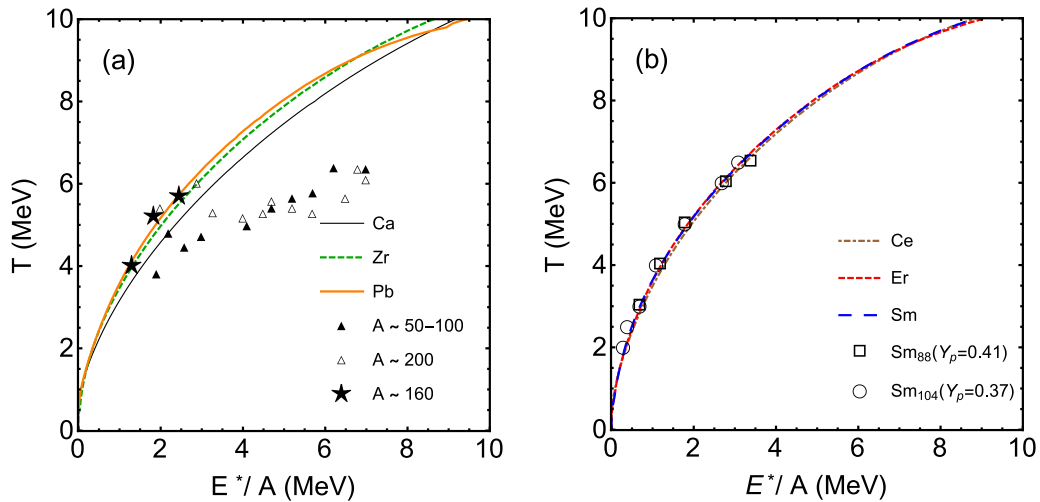
FIG. 12. Caloric curve for the (a) spherical and (b) deformed nuclei in the range of number of mass discussed in the text. (a) Experimental data from heavy ion collisions are shown for the mass number interval 50–100 [65] (full triangle), for a mass number of 200 [66] (open triangle), and for a mass number ~160 [67] (stars). (b) Results for $_{62}^{150}\text{Sm}_{88}$ calculated for a fixed proton fraction $Y_p = 0.41$ (square) and for $_{62}^{166}\text{Sm}_{104}$ calculated for a fixed proton fraction $Y_p = 0.37$ (circles).

ratio are larger. In Fig. 12(a) we compare the caloric curve obtained for spherical nuclei with experimental data of heavy ion collisions at higher energies for mass numbers between 50 and 100 from the EOS collaboration (full triangles) [65], mass number 200 (open triangles) [66], and mass number 160 (stars) [67]. In Fig. 12(b) we also plot calculations from [68] for the nucleus $_{62}^{150}\text{Sm}_{88}$ (open squares) for a fixed proton fraction $Y_p = 0.41$ and for the nucleus $_{62}^{166}\text{Sm}_{104}$ (open circles) for a fixed proton fraction $Y_p = 0.37$. In this figure our results are in agreement with calculations done in Ref. [68]. Our caloric curves of Fig. 12(a) agree reasonably well with the experimental data of [65–67] at temperatures up to 4 to 5 MeV and excitation energy from 1 to 3 MeV, but diverge from these at higher temperatures. However, such a result is not all that surprising. Our model takes into account only the neutrons and protons that have been emitted from the hot nucleus. One would expect that the emission of heavier particles, as well as multifragmentation, which begins to occur at temperatures of about 3 to 4 MeV, could substantially modify the relation between the excitation energy and the temperature.

V. CONCLUSION

In this work we have studied the effects of temperature on spherical and deformed nuclei in the Dirac-Hartree-Bogoliubov formalism. To investigate the nuclear structure we also take into account for the first time pairing and deformation calculated self-consistently. We analyze the effects of temperature on basic nuclear properties as well as on the thermodynamical properties of the caloric curve and entropy. We obtain self-consistent results for the temperature dependence of the pairing interaction within a relativistic formalism of the Dirac-Hartree-Bogoliubov theory [29,31]. In our approach, we use the NL3 parameter set as well as an additional parameter c_{pair}, which modifies the strength of the pairing interaction. We calculate the pairing energy, rms radii, nuclear spectra,

binding energy, excitation energy, caloric curves, and entropy for several spherical and deformed nucleus as a function of the temperature. We investigate the closed-shell spherical nuclei ^{40}Ca and ^{208}Pb, the open-shell spherical nuclei ^{90}Zr, ^{124}Sn, ^{140}Ce, and the deformed nuclei ^{150}Sm and ^{168}Er. We observe fluctuations in the mesonic potentials in the center of the nuclei in our calculations, an effect of the shell model, and find that these fluctuations disappear when the temperature increases. Furthermore, the strength of the mesonic and Coulomb potentials decreases with the increase of the temperature. For the case of the heavy nucleus ^{208}Pb, as temperature increases from $T = 0$ to $T = 4$ MeV, the energy change for each nuclear meson potential is $\Delta E \sim 45$ MeV for V_σ, $\Delta E \sim 50$ MeV for V_ω, $\Delta E \sim 5$ MeV for V_ρ, and $\Delta E \sim 0.5$ MeV for V_{coul}. We show that the rms radii, r_n, r_p, r_{ch}, and r_m, increase with the temperature.

We have studied the effects of temperature on the terms that contribute to the nuclear binding energy. We find that dependence on the temperature from the terms associated with the σ and ω meson potentials are almost the same: both increase in magnitude when the temperature grows. Thus since they have opposite signs their sum is almost independent of the temperature and of the same order of magnitude as the one-particle energy term E_{part}. The E_{part} term increases with temperature and is more sensitive to its changes, and it is the dominant term in the changing of the binding energy with temperature (see Fig. 1). The ρ meson potential is almost insensitive with change of the temperature and other terms increase slowly when the temperature grows. The total nuclear binding energy decreases with temperature and becomes positive when the nucleus becomes unbound. In general, the corresponding critical temperature is in the range $T \sim 8$–10 MeV.

In the case of open-shell spherical and deformed nuclei, we studied the role of temperature on the pairing interactions. In the cases of ^{124}Sn, ^{150}Sm, and ^{168}Er, we found that the

contribution of the pairing energy to the binding energy is initially large at $T = 0$ and becomes almost zero at temperatures of $T \sim 1$ MeV. We show that change of pairing fields with temperature is important, and must be taken into account in order to define the superfluidity and superconducting phase transitions. As shown in our formalism the normal density is a sum of two terms, one which can be loosely interpreted as the contribution of the states below the Fermi energy, now multiplied by a Fermi occupation factor. In addition, the other term which we can loosely interpret as the contribution of the states above the Fermi energy now appears multiplied by the Fermi factor of a positive-frequency state. When the pairing is zero, they reduce to the expected Fermi occupation factor. The contributions to the anomalous density are simply multiplied by the difference between the negative- and positive-energy Fermi occupations. The difference between the two factors decreases as the temperature increases, causing a reduction in the anomalous density and in the pairing. The pairing field maintains the initial deformation of deformed nuclei and reproduces the critical temperature (T_{c^p}) observed in experimental analysis of several deformed nuclei [6,61–63]. We found that the critical nuclear temperature for the superconducting to normal phase in the $^1S_0$ channel is quite low, and occurs in the range $T_{c^p} \sim$ 0.6–1.1 MeV. The superfluidity phase transition when $\Delta_{nn} \to 0$ occurs at smaller temperatures compared to the superconducting one. The superconducting phase transition occurs at $T_{c^p} = 1.03\Delta_{pp}(0)$ for ^{90}Zr, $T_{c^p} = 1.16\Delta_{pp}(0)$ for ^{140}Ce, $T_{c^p} = 0.92\Delta_{pp}(0)$ for ^{150}Sm, and $T_{c^p} = 0.97\Delta_{pp}(0)$ for ^{168}Er. The superfluidity phase transition occurs at $T_{c^p} = 0.72\Delta_{nn}(0)$ for ^{124}Sn, $T_{c^p} = 1.22\Delta_{nn}(0)$ for ^{150}Sm, and $T_{c^p} = 1.13\Delta_{nn}(0)$ for ^{168}Er. These relations for the critical temperature as a function of the proton and neutron gap at zero temperature are slightly larger than ones obtained in previous works, $T_{c^p} \sim 0.57\Delta_{pp}(0)$ and $T_{c^p} \sim 0.60\Delta_{nn}(0)$ as shown in Refs. [35,42]. The main reason for this difference comes from our pairing gap calculations that are relativistic and self-consistent, with the pairing interaction parameter $c_{\rm pair}$ chosen to reproduce the experimental results for $\Delta_{pp}(0)$ and $\Delta_{nn}(0)$ at zero temperature.

The shape transition for deformed nuclei occurs at higher temperatures in the range $T_{c^s} \sim 2.0$–4.0 MeV. This phase transitions can be clearly identified as a change in the slope of the entropy curve. The caloric curves for our calculations and their relation to the liquid-gas phase transition are also discussed. We found reasonable agreement between our curves and the experimental results shown in Refs. [1,2] at temperatures below 3–4 MeV. We encourage that more experimental studies be performed on excited nuclei, in order to better test our theoretical predictions.

[1] J. B. Natowitz, R. Wada, K. Hagel, T. Keutgen, M. Murray, A. Makeev, L. Qin, P. Smith, and C. Hamilton, Phys. Rev. C **65**, 034618 (2002).

[2] A. Kelić, J. B. Natowitz, and K.-H. Schmidt, Eur. Phys. J. A **30**, 203 (2006).

[3] H. A. Bethe, Rev. Mod. Phys. **9**, 69 (1937).

[4] V. Weisskopf, Phys. Rev. **52**, 295 (1937).

[5] E. Suraud, Ch. Grégoire, and B. Tamain, Prog. Part. Nucl. Phys. **23**, 357 (1989).

[6] M. Guttormsen, A. Bjerve, M. Hjorth-Jensen, E. Melby, J. Rekstad, A. Schiller, S. Siem, and A. Belić, Phys. Rev. C **62**, 024306 (2000).

[7] W. Trautmann, Nucl. Phys. A **685**, 233 (2001).

[8] C. Sfienti *et al.* (ALADIN2000 Collaboration), Phys. Rev. Lett. **102**, 152701 (2009).

[9] P. Bonche, S. Levit, and D. Vautherin, Nucl. Phys. A **427**, 278 (1984).

[10] P. Bonche, S. Levit, and D. Vautherin, Nucl. Phys. A **436**, 265 (1985).

[11] E. Suraud, Nucl. Phys. A **462**, 109 (1987).

[12] M. Brack and P. Quentin, Phys. Scr. **10**, 163 (1974).

[13] M. Brack and P. Quentin, Phys. Lett. B **52**, 159 (1974).

[14] D. Gogny, *Proceedings of the International Conference on Nuclear Self-consistent Fields*, Trieste 1975, edited by G. Ripka and M. Porneuf (North-Holland, Amsterdam, 1975).

[15] J. Decharge and D. Gogny, Phys. Rev. C **21**, 1568 (1980).

[16] B. V. Carlson and T. Frederico, IEAV Report No. IEAv/NT05-89, 1989.

[17] H. Kucharek and P. Ring, Z. Phys. A **339**, 23 (1991).

[18] L. P. Gor'kov, ZhETF **34**, 735 (1958) [Sov. Phys. JETP **7**, 505 (1958)].

[19] F. B. Guimarães, B. V. Carlson, and T. Frederico, Phys. Rev. C **54**, 2385 (1996).

[20] F. Matera, G. Fabbri, and A. Dellafiore, Phys. Rev. C **56**, 228 (1997).

[21] B. V. Carlson, T. Frederico, and F. B. Guimarães, Phys. Rev. C **56**, 3097 (1997).

[22] B. V. Carlson and D. Hirata, Phys. Rev. C **62**, 054310 (2000).

[23] I. Tanihata, H. Hamagaki, O. Hashimoto, Y. Shida, N. Yoshikawa, K. Sugimoto, O. Yamakawa, T. Kobayashi, and N. Takahashi, Phys. Rev. Lett. **55**, 2676 (1985).

[24] I. Tanihata *et al.*, Phys. Lett. B **160**, 380 (1985).

[25] J. Meng and P. Ring, Phys. Rev. Lett. **77**, 3963 (1996).

[26] J. Meng, Nucl. Phys. A **635**, 3 (1998).

[27] J. Meng, H. Toki, S. G. Zhou, S. Q. Zhang, W. H. Long, and L. S. Geng, Prog. Part. Nucl. Phys. A **57**, 470 (2006).

[28] S. G. Zhou, J. Meng, P. Ring, and E. G. Zhao, Phys. Rev. C **82**, 011301 (2010).

[29] R. Lisboa, Ph.D. thesis (in Portuguese), Universidade Federal Fluminense, Niter, 2007.

[30] R. Lisboa, M. Malheiro, and B. V. Carlson, Int. J. Mod. Phys. E **16**, 3032 (2007).

[31] R. Lisboa, M. Malheiro, and B. V. Carlson, Nucl. Phys. B, Proc. Suppl. **199**, 345 (2010).

[32] Y. K. Gambhir, J. P. Maharana, G. A. Lalazissis, C. P. Panos, and P. Ring, Phys. Rev. C **62**, 054610 (2000).

[33] A. L. Goodman, Nucl. Phys. A **352**, 30 (1981).

[34] A. L. Goodman, Phys. Rev. C **33**, 2212 (1986).

[35] A. L. Goodman, Phys. Rev. C **34**, 1942 (1986).

[36] J. L. Egido, L. M. Robledo, and V. Martin, Phys. Rev. Lett. **85**, 26 (2000).

[37] Y. F. Niu, Z. M. Niu, N. Paar, D. Vretenar, G. H. Wang, J. S. Bai, and J. Meng, Phys. Rev. C **88**, 034308 (2013).

[38] J. F. Berger, M. Girod, and D. Gogny, Comput. Phys. Commun. **63**, 365 (1991).

[39] Y. Tian, Z. Y. Ma, and P. Ring, Phys. Lett. B **676**, 44 (2009).

[40] P. W. Zhao, Z. P. Li, J. M. Yao, and J. Meng, Phys. Rev. C **82**, 054319 (2010).

[41] E. Yüksel, E. Khan, and K. Bozkurt, J. Phys.: Conf. Ser. **533**, 012019 (2014).

[42] J. J. Li, J. Margueron, W. H. Long, and N. VanGiai, Phys. Rev. C **92**, 014302 (2015).

[43] G. A. Lalazissis, J. König, and P. Ring, Phys. Rev. C **55**, 540 (1997).

[44] T. Matsubara, Prog. Theor. Phys. **14**, 351 (1955).

[45] L. N. Cooper, Phys. Rev. **104**, 1189 (1956).

[46] M. Baldo, U. Lombardo, and P. Schuck, Phys. Rev. C **52**, 975 (1995).

[47] V. A. Khodel, V. V. Khodel, and J. W. Clark, Nucl. Phys. A **598**, 390 (1996).

[48] Ø. Elgarøy, L. Engvik, M. Hjorth-Jensen, and E. Osnes, Nucl. Phys. A **604**, 466 (1996).

[49] D. Vautherin and D. M. Brink, Phys. Rev. C **5**, 626 (1972).

[50] Y. K. Gambhir, P. Ring, and A. Thimet, Ann. Phys. (NY) **198**, 132 (1990).

[51] G. A. Lalazissis, D. Vretenar, and P. Ring, Phys. Rev. C **57**, 2294 (1998).

[52] D. Vretenar, G. A. Lalazissis, and P. Ring, Phys. Rev. C **57**, 3071 (1998).

[53] G. A. Lalazissis, D. Vretenar, P. Ring, M. Stoitsov, and L. Robledo, Phys. Rev. C **60**, 014310 (1999).

[54] M. Abramowitz and I. A. Stegun, *Handbook of Mathematical Functions* (Dover, New York, 1970).

[55] S. R. Souza, B. V. Carlson, R. Donangelo, W. G. Lynch, A. W. Steiner, and M. B. Tsang, Phys. Rev. C **79**, 054602 (2009).

[56] J. Meng, W. Zhang, S. G. Zhou, H. Toki, and L. S. Geng, Eur. Phys. J. A **25**, 23 (2005).

[57] C. Providência, D. P. Menezes, and L. Brito, Nucl. Phys. A **703**, 188 (2001).

[58] G. Audi and A. H. Wapstra, Nucl. Phys. A **595**, 409 (1995).

[59] P. Möller, J. R. Nix, W. D. Myers, and W. J. Swiatecki, At. Data Nucl. Data Tables **61**, 127 (1995).

[60] L. S. Geng, H. Toki, and J. Meng, Mod. Phys. Lett. A **19**, 2171 (2004).

[61] M. Guttormsen, M. Hjorth-Jensen, E. Melby, J. Rekstad, A. Schiller, and S. Siem, Phys. Rev. C **63**, 044301 (2001).

[62] M. Guttormsen, M. Hjorth-Jensen, E. Melby, J. Rekstad, A. Schiller, and S. Siem, Phys. Rev. C **64**, 034319 (2001).

[63] R. Chankova, A. Schiller, U. Agvaanluvsan, E. Algin, L. A. Bernstein, M. Guttormsen, F. Ingebretsen, S. Costa, J. B. Elliott, M. L. Gilkes *et al.*, Phys. Rev. C **73**, 034311 (2006).

[64] K. Kaneko, M. Hasegawa, U. Agvaanluvsan, E. Algin, R. Chankova, M. Guttormsen *et al.*, Phys. Rev. C **74**, 024325 (2006).

[65] J. A. Hauger, S. Albergo, F. Bieser, F. P. Brady, Z. Caccia, D. A. Cebra, A. D. Chacon, J. L. Chance, Y. Choi *et al.*, Phys. Rev. Lett. **77**, 235 (1996).

[66] J. Pochodzalla, T. Mohlenkamp, T. Rubehn, A. Schuttauf, A. Worner, E. Zude *et al.*, Phys. Rev. Lett. **75**, 1040 (1995).

[67] K. Hagel, D. Fabris, P. Gonthier, H. Ho, Y. Lou, Z. Majka, G. Mouchaty, M. N. Namboodiri, J. B. Natowitz, G. Nebbia *et al.*, Nucl. Phys. A **486**, 429 (1988).

[68] D. P. Menezes and C. Providência, Phys. Rev. C **64**, 044306 (2001).